A dissemination-prone morphotype enhances extrapulmonary organ entry by the fungus *Cryptococcus neoformans*

Steven T. Denham[1], Brianna Brammer[1], Krystal Y. Chung[1], Morgan A. Wambaugh[1], Joseph M. Bednarek[1], Li Guo[2], and Jessica C.S. Brown[1*]

[1]Division of Microbiology and Immunology, Department of Pathology, University of Utah, Salt Lake City, UT 84112, USA

[2]Molecular Medicine Program, University of Utah, Salt Lake City, UT 84112, USA

*Correspondence:: jessica.brown@path.utah.edu

SUMMARY:

Environmental pathogens, which move from ecological niches to mammalian hosts, must adapt to dramatically different environments. Microbes that disseminate farther, including the fungal meningitis pathogen *Cryptococcus neoformans*, require additional adaptation to diverse tissues. When *C. neoformans* enters the lungs, infecting cells (<10 μm diameter) enlarge (>30 μm diameter), then form a heterogeneous population. The brain contains uniformly small cells (~7 μm). We demonstrate that formation of a small *C. neoformans* morphotype – called "seed" cells due to their disseminating ability – is critical for extrapulmonary organ entry. Seed cell formation is triggered by environmental factors, including *C. neoformans*' environmental niche, pigeon guano. The underlying trigger, phosphate, can be released by tissue damage, potentially establishing a feed-forward loop of seed cell formation and dissemination. We demonstrate that *C. neoformans*' size variation is not just a continuum but inducible subpopulations that change host interactions to facilitate microbe survival and spread.

INTRODUCTION:

Environmental pathogens must be able to adapt to a wide variety of conditions as they transition from their ecological niches to host infection. This is particularly challenging for pathogens that cause disseminated disease, such as the primary cause of fungal meningitis, *Cryptococcus neoformans* (Rajasingham et al., 2017). As disseminating pathogens such as *C. neoformans* escape from the lungs, they must evade the immune system (Bojarczuk et al., 2016; Bulmer and Sans, 1967; Chun et al., 2011; Luberto et al., 2003; Okagaki et al., 2010; Stano et al., 2009; Walsh et al., 2019; Zaragoza et al., 2010), survive in the bloodstream and/or host cells (Botts and Hull, 2010; Charlier et al., 2009; Diamond and Bennett, 1973; Feldmesser et al., 2000; Gaylord et al., 2020; Walsh et al., 2019), and finally enter and grow in the brain (Chang et al., 2004; Chen et al., 2003; Chen et al., 2021; Huang et al., 2011; Liu et al., 2013;

35 Liu et al., 2014; Maruvada et al., 2012; Olszewski et al., 2004; Santiago-Tirado et al., 2017; Vu
36 et al., 2013).
37 Many microbes employ phenotypic switching and/or phenotypic heterogeneity to survive
38 in complex and fluctuating host environments (Altamirano et al., 2020; Weigel and Dersch,
39 2018). These strategies include the antigen switching employed by bacterial species (spp.)
40 including *Neisseria* spp. (Haas and Meyer, 1986; Swanson et al., 1986), *Borrelia burdorferi*
41 (Chaconas et al., 2020), and parasites such as *Plasmodium* spp. (Roberts et al., 1992; Smith et
42 al., 1995), which allow the infecting organism to avoid adaptive host immune responses. Among
43 fungi, *Candida albicans* adjust exposure levels of β-glucan (Ballou et al., 2016), which is readily
44 detected by the host (Brown et al., 2003; Gow et al., 2007).
45 Another strategy is phenotypic heterogeneity (Altamirano et al., 2020), a mechanism of
46 bet-hedging against environmental stressors, including host responses that can occur within
47 single foci of infection (Davis, 2018). For example, microbial cells at the perimeter of infection
48 foci may be more open to attack from immune cells, while the core may be depleted of nutrients
49 and oxygen (Davis et al., 2015; Kowalski et al., 2019). Variation within populations provide
50 phenotypic robustness and can also influence which cells in a localized population are more
51 likely to spread to new sites within a host, a phenomenon that significantly impacts the likelihood
52 and trajectory of cancer metastasis (San Juan et al., 2019). Fungi have long been known to
53 undergo dramatic phenotypic changes that influence disease, such as the yeast / hyphal
54 switches of dimorphic fungi (Garfoot et al., 2016; Guimarães et al., 2011; Kanetsuna and
55 Carbonell, 1971; Mukaremera et al., 2017; Viriyakosol et al., 2013; Whiston et al., 2012),
56 spherule development in *Coccidioides* spp. (Viriyakosol et al., 2013; Whiston et al., 2012), and
57 sporulation of conidia in *Aspergillus* spp. (Aimanianda et al., 2009; Hohl et al., 2005). The
58 differences between yeast and filamentous forms are dramatic and superficially obvious due to
59 their extreme morphological differences. However, we are only beginning to understand that
60 more subtle variations within morphological states can have profound influences on host
61 infectivity (Pande et al., 2013; Tao et al., 2014). The model human fungal pathogen
62 *Cryptococcus neoformans* grows primarily as a budding yeast, with a filamentous form generally
63 associated with mating and not virulence (Wang et al., 2012). Here we use the seemingly subtle
64 differences between different yeast forms of *C. neoformans* to address the role that phenotypic
65 heterogeneity plays in intra-host dissemination.
66 A ubiquitous saprophytic fungus associated with trees and bird guano (Emmons, 1955;
67 Lazera et al., 1996), *C. neoformans* is generally harmless, with human exposure thought to be
68 as high as 70% by age five (Goldman et al., 2001). Infection follows inhalation of a fungal cell or

69 spore (Maziarz and Perfect, 2016), and in immunocompromised individuals *C. neoformans*
70 disseminates via the bloodstream and/or lymphatics to almost any organ in the body (Lin et al.,
71 2015; Maziarz and Perfect, 2016). *C. neoformans* cells rapidly proliferate in the central nervous
72 system, and the resulting fungal meningoencephalitis drives cryptococcosis patient mortality,
73 killing ~180,000 people each year worldwide (Rajasingham et al., 2017).
74 *C. neoformans* is an excellent model organism to study the impact of phenotypic
75 heterogeneity on intra-host dissemination. Two of its primary virulence attributes—cell and
76 capsule size—vary considerably during infection and are readily observable via microscopy and
77 flow cytometry (Li and Nielsen, 2017). Isolates belonging to the *Cryptococcus* genus exhibit a
78 high degree of cell and capsule size diversity, and morphological heterogeneity strongly impacts
79 *C. neoformans* virulence: increased capacity for morphological variation among isolates
80 correlates with worse clinical outcome (Fernandes et al., 2018).
81 Cell and capsule size are finely tuned to a multitude of environmental signals and impact
82 stress resistance, immune recognition, and overall pathogenesis (Casadevall et al., 2019;
83 O'Meara and Alspaugh, 2012). Cells grown in nutrient replete laboratory media are
84 morphologically homogeneous (5–10 μm in total (cell + capsule) diameter) and poorly
85 encapsulated (O'Meara and Alspaugh, 2012), while fungal cells proliferating in the lungs are
86 morphologically heterogeneous (1-100 μm in total diameter) and encapsulated, although
87 capsule thickness varies considerably (Wang and Lin, 2015; Zaragoza, 2011). In the host, the
88 polysaccharide capsule shields immunostimulatory microbe-associated molecular patterns in
89 the fungal cell wall, suppresses phagocytosis, and protects against oxidative stress (Casadevall
90 et al., 2019; O'Meara and Alspaugh, 2012).
91 The best understood *C. neoformans* morphotype is the polyploid (≥4C) “titan” cell,
92 measuring 10-100 μm in cell body diameter (Dambuza et al., 2018; Hommel et al., 2018;
93 Okagaki and Nielsen, 2012; Okagaki et al., 2011; Trevijano-Contador et al., 2018; Zaragoza et
94 al., 2010; Zhou and Ballou, 2018). Titans are more resistant to phagocytosis and oxidative
95 stress and skew immunity toward a non-protective Th2 response (Crabtree et al., 2012; Okagaki
96 and Nielsen, 2012; Okagaki et al., 2010).
97 While titans contribute considerably to cryptococcal pathogenesis, they are not the only
98 morphotype present during infection, accounting for a minority of cryptococcal cells within the
99 lungs (Zhou and Ballou, 2018). Tissue-specific differences in cryptococcal morphology also
100 manifest in human patients and animal infection models (Denham et al., 2018; Rivera et al.,
101 1998; Xie et al., 2012). Titan cells are rarely observed outside of the lungs, and overall cell and
102 capsule sizes tend to be substantially smaller in extrapulmonary sites, including the brain

103 (Charlier et al., 2005; Denham et al., 2018; Rivera et al., 1998; Xie et al., 2012). While the *C.*
104 *neoformans* populations in extrapulmonary organs appear to become heterogeneous over time
105 (Lee et al., 1996), the *C. neoformans* population that appears early in the mouse model
106 dissemination process is striking in its homogeneity and small median size (Denham et al.,
107 2018; Fernandes et al., 2018; Fernandes and Carter, 2020; Fernandes et al., 2016; Zaragoza,
108 2011). We therefore hypothesize that smaller morphotypes are more likely to disseminate and
109 enter extrapulmonary organs.
110
111 **RESULTS:**
112 **Small cell formation correlates with extrapulmonary dissemination and varies with strain**
113 **and *Cryptococcus* species**
114 *Cryptococcus* spp. isolates vary in their capacity for morphological variation (Fernandes
115 et al., 2018). To more broadly assess morphological shifts during infection, we inoculated ~8-
116 week-old female B6 mice with a panel of common *Cryptococcus* spp. reference strains ($2.5x10^4$
117 cells / mouse). At 3 and 17 days post-inoculation (dpi), we homogenized lungs and measured
118 fungal cell body and capsule size (**Figures 1A and 1B**). Morphogenesis varied widely among
119 *Cryptococcus* isolates. While KN99 (*C. neoformans*) and Bt63 (*C. neoformans*) cells shifted
120 smaller between 3 and 17 dpi, R265 (*C. deuterogattii*) and WM276 (*C. gattii*) continued to
121 increase in size—largely due to increased capsule thickness. Smaller median cell size at 17 dpi
122 correlated with increased extrapulmonary burden (**Figures 1C and 1D**). These data suggest
123 that among *Cryptococcus* isolates, the emergence of small cells (<10 μm) within the lungs is a
124 strong predictor of extrapulmonary dissemination.
125 We also measured cell and capsule size in the blood, liver, spleen, and brains of mice
126 inoculated with KN99 cells (the most widely used reference strain) (**Figure 1E**). The range of
127 cell size in the blood and liver was surprisingly broad considering that murine microcapillaries
128 can be as small as 3.5 μm. Although rare, we did find fungal cells in the blood measuring 50 μm
129 across. However, median total diameter in the blood at 17 dpi was 12.72 μm, which was
130 noticeably smaller than earlier timepoints in the lungs (27.21 μm at 3 dpi and 18.71 μm at 14
131 dpi) indicating that entry into the blood may still be a size-limiting bottleneck. In contrast, cell
132 size in the spleen and brain was far more restricted. The vast majority of cells in the spleen
133 were <15 μm, while cells in the brain rarely exceeded 10 μm in total diameter. These data
134 suggest that the ability to form small cells/capsules in the lungs is a strong predictor of
135 extrapulmonary dissemination, and that multiple bottlenecks may restrict vascular
136 dissemination.

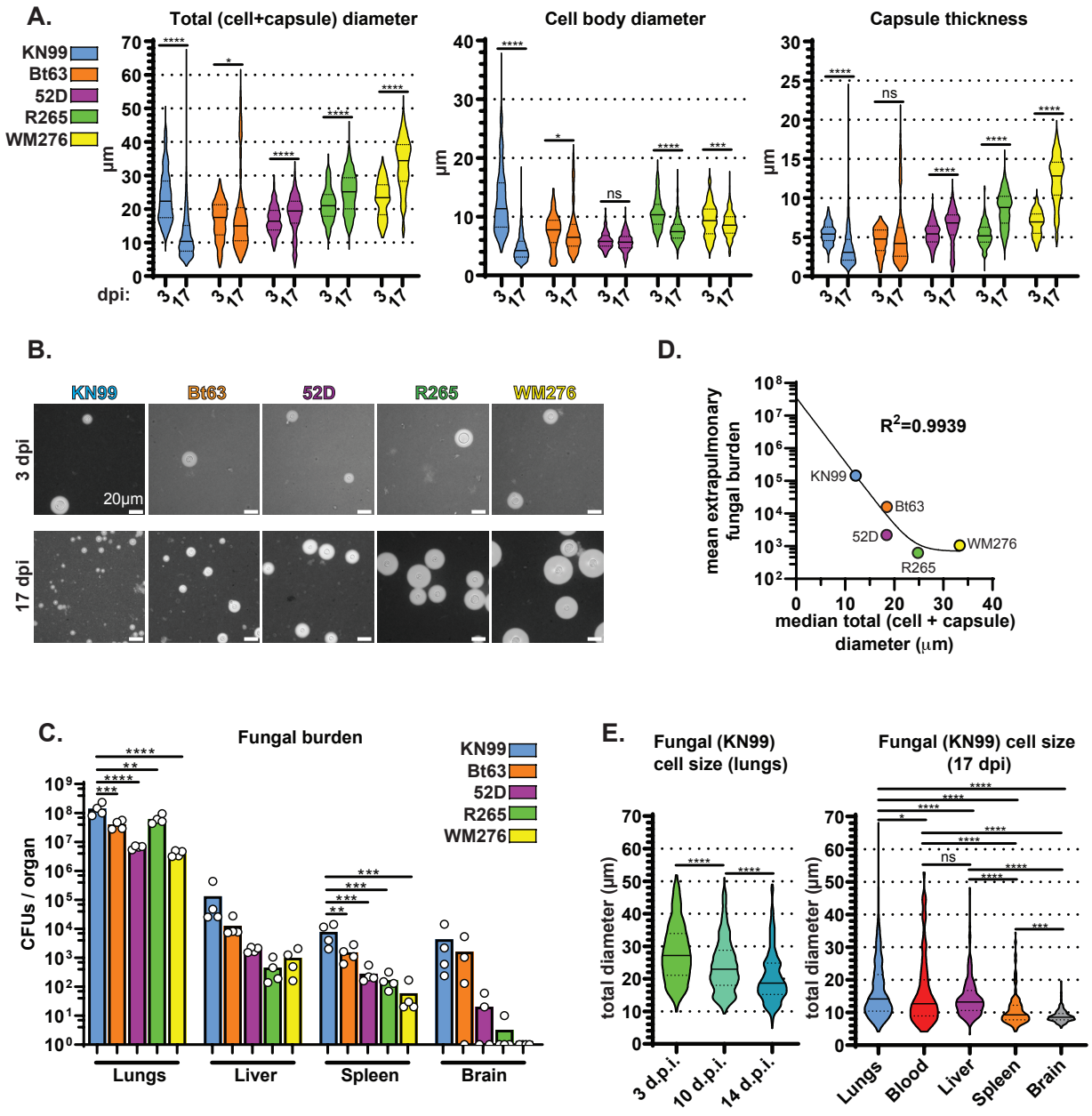

Figure 1: Morphological transitions during pulmonary infections correlate with fungal dissemination. (A) Total (cell+capsule) diameter, cell body diameter, and capsule thickness

140 measurements at 3 and 17 days post-intranasal inoculation (dpi) of mice (Mann-Whitney U test;
141 N=4 mice per timepoint, 57-65 fungal cells measured per mouse at 3 dpi and 117-266 fungal
142 cells per mouse at 17 dpi). Solid lines in the violin plots indicate the median and dotted lines
143 mark quartiles. **(B)** Representative India ink images of fungal cells quantified in 1A. **(C)** Fungal
144 burden in mice at 17 dpi (One-way ANOVA and uncorrected Fisher's LSD). The bar graph
145 represents the mean. **(D)** Nonlinear regression of mean extrapulmonary (liver + spleen + brain)
146 fungal burden and median total (cell + capsule) diameter. **(E)** Total diameter in KN99-infected
147 lungs at 3, 10, and 14 dpi and total diameter in KN99-infected organs at 17 dpi (Mann-Whitney
148 U-test; N=4 mice per timepoint; fungal cells measured per mouse in the lungs: 275, blood: 38,
149 liver: 72, spleen: 43, brain: 72). Solid lines in the violin plots indicate the median and dotted lines
150 mark quartiles. All panels in Figure 1: ns: not significant *$p<0.05$; **$p<0.01$; ***$p<0.001$;
151 ****$p<0.0001$.
152

153 **Inoculum size affects the rate of morphological shift**

154 Lower initial cell density increases the frequency of titan cell formation *in vitro* (Trevijano-
155 Contador et al., 2018) and *in vivo* (Okagaki et al., 2010). We hypothesized that reducing the
156 number of cells in the inoculum would increase the frequency of larger cells early in lung
157 infection and slow the rate of small cell formation (**Figures S1A, S1B, and S1C**). We inoculated
158 mice with 10^3, 10^4, or 10^5 KN99-mCherry cells per mouse and employed the flow cytometry
159 forward scatter-area (FSC-A) parameter as a high-throughput assay to estimate relative
160 changes in cell size at 3, 7, 10, 14, and 17 dpi.

161 Consistent with our hypothesis, inoculating mice with fewer fungal cells increased fungal
162 cell size at 3 dpi, decreased the rate of cell size reduction in the lungs (**Figures S1A, S1B, and**
163 **S1C**), decreased lung fungal burden (**Figure S1D**), and decreased dissemination to the brain at
164 17 dpi (**Figure S1E**). Therefore, lower initial fungal cell density slows the rate at which fungal
165 cells shift smaller in the lungs and disseminate to the brain.

166

167 **Populations of cells isolated from the lungs display size-dependent differences in cell**
168 **surface features and differentially bind host factors**

169 When we compared the labor-intensive microscopy-based measurements of cell size
170 with flow cytometry-based measurements, we still observed a fungal size shift over the course
171 of infection (**Figure S1A**). Thus, we sought to isolate KN99-mCherry cells from infected lung
172 tissue (14 dpi) via fluorescence-activated cell sorting (FACS) using forward scatter area (FSC-
173 A) as a stand-in for size. We sorted cross-sections of the fungal cell size distribution
174 corresponding to the smallest (small *ex vivo*: median total diameter of 7.6 μm), intermediate
175 (mid *ex vivo*: median total diameter of 14.0 μm), and largest (large *ex vivo*: median total
176 diameter of 21.8 μm) ~20% of the population (**Figure 2A**). We further confirmed that we isolated
177 distinct populations based on cell and capsule size (**Figure 2B**). Fungal cells sorted from each
178 gate were also equivalently viable (**Figure 2C**).

179 We then measured DNA ploidy with 4′,6-diamidino-2-phenylindole (DAPI) staining
180 (**Figure 2D**). We used haploid cells cultured in minimal yeast nitrogen base (YNB) medium +/-
181 benomyl as a control, since benomyl inhibits cell division and traps cells at 2C (Jacobs et al.,
182 1988). Cells with >2C content are considered titan cells. Only the large *ex vivo* population
183 contained an appreciable number of titan cells (mean: 21.4% >2C) (**Figure S2**). Intermediate *ex*
184 *vivo* cells averaged 74.2% 1C and 22.8% 2C, while small *ex vivo* cells averaged 89.2% 1C and
185 10.0% 2C.

186

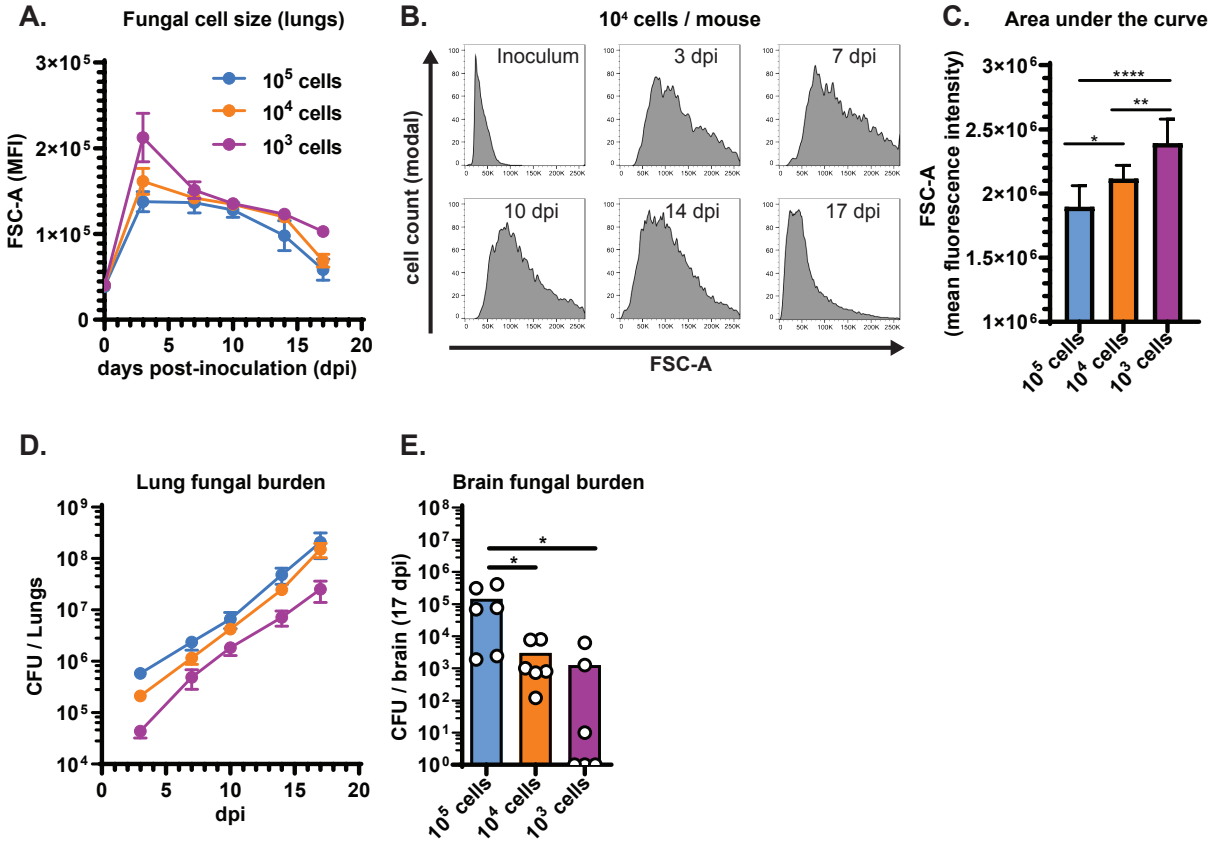

Supplemental Figure 1: Inoculum size alters the rate at which *C. neoformans* populations shift toward smaller cell size in the lungs and disseminate to the brain. (A) We inoculated mice with the indicated number of KN99-mCherry cells. The line graph shows the forward scatter-area (FSC-A) measurements at the indicated days post-inoculation (dpi), which estimates relative fungal size in the lungs (N=6 mice per timepoint). Points indicate the mean and the error bars indicate standard deviation. **(B)** Representative flow cytometry plots from mice inoculated with 10^4 KN99-mCherry cells / mouse. **(C)** Quantification of the area under the curve for the curves displayed in Figure S1A. Bar graphs display the mean fluorescence intensity and error bars indicate standard deviation. **(D)** Lung fungal burden in the same mice described in Figure S1A and quantified by colony forming units (CFU). **(E)** Brain fungal burden in mice at 17 dpi quantified by CFUs. Bar graphs display the mean. All comparisons in Figure S1 were analyzed using one-way ANOVA and uncorrected Fisher's LSD (ns: not significant; *p<0.05; **p<0.01; ***p<0.001; ****p<0.0001).

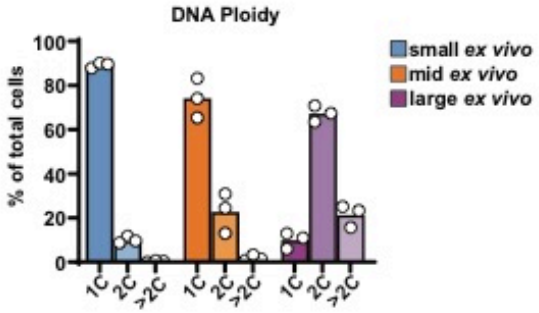

Supplemental Figure 2: DNA content of *ex vivo C. neoformans* populations. Percentage of cells with 1C, 2C, and >2C DNA content in the indicated population. Values correspond to the representative flow cytometry plot in Figure 2D. Bar graphs display the mean.

207 **Small *ex vivo* cells disseminate to extrapulmonary organs at a higher rate than**
208 **intermediate and large *ex vivo* cells**
209 Most infection models—including intravenous dissemination models—use *C.*
210 *neoformans* yeast cells collected from nutrient replete laboratory media as the inoculum
211 (Mukaremera et al., 2019; Ngamskulrungroj et al., 2012; Sabiiti et al., 2012), failing to capture
212 the phenotypic heterogeneity generated during lung infection. Here we accounted for
213 phenotypic heterogeneity generated during lung infection by isolating cells directly from infected
214 lung tissue and sorting them according to size. To directly address the impact of fungal cell and
215 capsule size on dissemination, we intravenously inoculated naïve mice with small, intermediate,
216 and large *ex vivo* cells (10^5 cells / mouse). With blood flow from the tail vein running directly to
217 the heart and then lungs for reoxygenation, the lungs harbor the first major bed of
218 microcapillaries fungal cells are likely to encounter following tail vein inoculation. Therefore,
219 sorting fungal cells from infected lung tissue prior to tail vein inoculation roughly replicates the
220 fate of fungal cells had they entered the bloodstream from the lungs. Consistent with our
221 hypothesis, a greater number of small *ex vivo* cells reached the liver, spleen, and brain by 3
222 hours post-inoculation (hpi) than intermediate and large *ex vivo* cells (**Figure 2E**). In contrast,
223 the majority of intermediate and large *ex vivo* cells remained in the lungs at 3 hpi, possibly
224 because they failed to navigate the lung microcapillaries as well as small *ex vivo* cells. We
225 observed the same trends in fungal burden at 3 dpi, indicating that small *ex vivo* cells are well-
226 capable of proliferating in extrapulmonary tissues (**Figure 2F**).
227 Although brain fungal burden was equivalent in mice inoculated with intermediate and
228 large *ex vivo* cells at 3 hpi, there were more mid *ex vivo* cells in the brain by 3 dpi. We asked
229 whether the reduced brain fungal burden in mice inoculated with large *ex vivo* cells was due to
230 inefficient blood-brain barrier crossing or reduced proliferation in the brain. To estimate blood-
231 brain barrier crossing *in vivo*, we intracardially perfused mice at 3 hpi to drive out circulating
232 fungal cells and normalized the fungal burden in perfused mice to nonperfused mice inoculated
233 on the same day. While perfusion did not significantly affect brain fungal burden in mice
234 inoculated with small or mid *ex vivo* cells, perfusion drove nearly all of the large *ex vivo* cells
235 from the brain (**Figure 2G**). In contrast, fungal burden post-intracranial inoculation was
236 independent of initial fungal cell size (**Figure 2H**), suggesting that while large *ex vivo* cells are
237 poorer at reaching the brain and crossing the blood-brain barrier, they are not deficient at
238 proliferating in the brain.
239

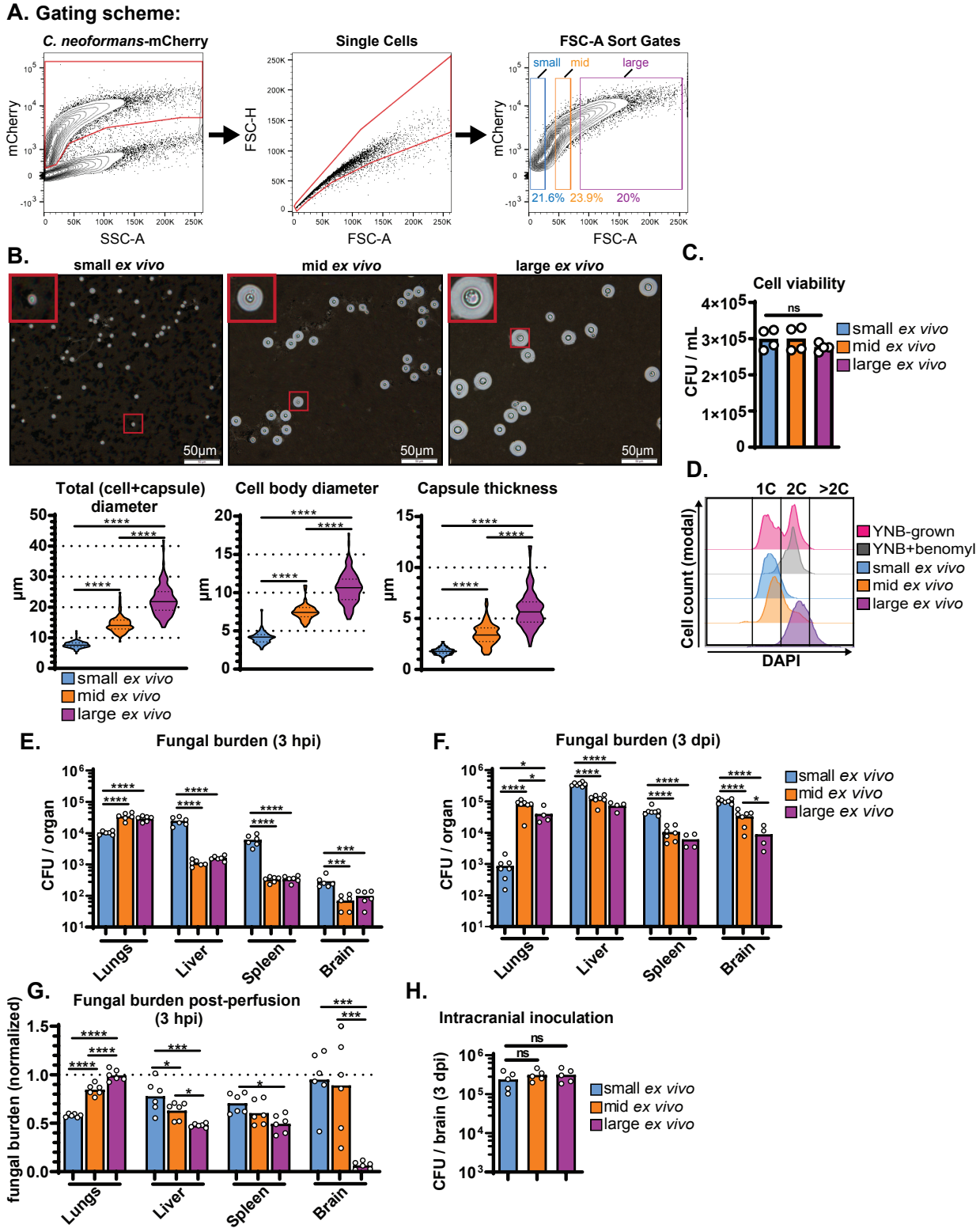
A. Gating scheme:
C. neoformans-mCherry
Single Cells
FSC-A Sort Gates
mCherry
SSC-A
FSC-H
FSC-A
small
mid
large
21.6%
23.9%
20%
B.
small ex vivo
mid ex vivo
large ex vivo
50µm
C.
Cell viability
CFU / mL
ns
small ex vivo
mid ex vivo
large ex vivo
D.
1C
2C
>2C
Cell count (modal)
DAPI
YNB-grown
YNB+benomyl
small ex vivo
mid ex vivo
large ex vivo
Total (cell+capsule) diameter
Cell body diameter
Capsule thickness
µm
small ex vivo
mid ex vivo
large ex vivo
E.
Fungal burden (3 hpi)
CFU / organ
Lungs
Liver
Spleen
Brain
F.
Fungal burden (3 dpi)
CFU / organ
small ex vivo
mid ex vivo
large ex vivo
G.
Fungal burden post-perfusion (3 hpi)
fungal burden (normalized)
H.
Intracranial inoculation
CFU / brain (3 dpi)

240

241 **Figure 2: Sorting and characterization of fungal populations from infected lungs. (A)**
242 FACS gating scheme for sorting KN99-mCherry cells from infected mouse lungs into
243 populations of “small”, “mid”, and “large” cells using forward scatter-area (FSC-A) to
244 approximate size. **(B)** Representative India ink images of cells sorted from “small”, “mid”, and
245 “large FSC-A gates and cell/capsule size measurements (N=97-120 fungal cells). Solid lines in
246 the violin plots indicate the median and dotted lines mark quartiles. **(C)** Cell viability post-sort
247 quantified by colony-forming unit (CFU) count (N=4). **(D)** Representative flow plot of DNA-
248 content measured with DAPI staining. YNB (minimal YNB medium). **(E)** Fungal burden,
249 measured by colony forming unit counts (CFU), at 3 hours post-inoculation (hpi) and 3 days **(F)**
250 post-inoculation (dpi) in mice intravenously-inoculated with small, mid, or large *ex vivo* cells
251 (One-way ANOVA and uncorrected Fisher’s LSD). **(G)** Fungal burden in mice inoculated with
252 sorted *ex vivo* fungal cells and perfused at 3 hpi. Fungal burden was normalized to inoculated,
253 but non-perfused control mice (Mann-Whitney U-test). **(H)** Fungal burden at 3 dpi in mice
254 intracranially inoculated with sorted *ex vivo* fungal cells (One-way ANOVA and uncorrected
255 Fisher’s LSD).
256

257 **Cell surface differences between *ex vivo* populations result in uptake of small *ex vivo***
258 **cells by macrophages**
259 Morphological changes in *C. neoformans* are often accompanied by alterations in cell
260 surface architecture and immune recognition. We screened the binding rate (% total fungal cells
261 bound) of a panel of soluble receptors to small, intermediate, and large *ex vivo* cells (**Figure**
262 **3A**). Large *ex vivo* cells were more likely to be bound by complement protein C3 than
263 intermediate, or small *ex vivo* cells ($p < 0.05$). In contrast, small and intermediate *ex vivo* cells
264 were more likely to be bound by lung surfactant protein D (SPD) ($p < 0.01$). SPD binding to *C.*
265 *neoformans* is deleterious for the host, potentially because SPD agglutinates fungal cells and
266 disrupts fungal clearance by macrophages (Geunes-Boyer et al., 2012). We saw low-level ,
267 uniform binding of IgA and IgM class antibodies, and little to no binding by mannose-binding
268 lectins.
269 Differences in host factor binding suggested that cell surface architecture may differ
270 among the sorted populations. We used two lectins to probe the exposure of microbial features
271 in different layers of the cell wall: wheat germ agglutinin (WGA), which recognizes chitin in the
272 innermost layers of the cryptococcal cell wall and concanavalin A, which binds mannose on
273 mannoproteins in the outer cell wall and inner capsule. There were no significant differences in
274 chitin exposure as measured by flow cytometry (**Figure 3B**). However, mannose was
275 significantly more exposed on small *ex vivo* cells compared with intermediate and large *ex vivo*
276 cells and cells grown in non-capsule inducing minimal YNB medium (**Figure 3C**).
277 We visualized mannose exposure patterns via microscopy and characterized staining as
278 negative, punctate (one or more distinct staining puncta), diffuse (staining covers the observable
279 cell surface), or both punctate and diffuse (**Figure 3D**). Mannose was more likely to be exposed
280 both at specific puncta and diffusely across the surface of small *ex vivo* cells. Mannose
281 exposure can correspond to recent bud scars, which may explain the punctate staining in our
282 analysis (Panepinto et al., 2007). The high prevalence of diffuse mannose exposure on small
283 cells may be due to their relatively thin capsules. Altogether, these results suggest that cell and
284 capsule size heterogeneity correlates with heterogeneity in cell surface architecture and
285 immune recognition.
286 As small *ex vivo* cells most efficiently disseminated to extrapulmonary organs, we
287 examined the mechanisms governing their dissemination profile more closely. Most small *ex*
288 *vivo* cells that made it past the lungs at 3 hpi were cleared in the liver and spleen (**Figure 3E**).
289 The liver plays a major role in clearing microbes and microbial components from the blood
290 (Macpherson et al., 2016) via recognition of microbial-associated molecular patterns (MAMPs)

291 (Kubes and Jenne, 2018). Recently, intravital imaging revealed that liver macrophages clear *C.*
292 *neoformans* cells from the bloodstream (Sun et al., 2019). However, the inoculum for those
293 studies consisted of *C. neoformans* cells cultured *in vitro*. Our cell surface characterization
294 revealed that small *ex vivo* cells differ from cells cultured *in vitro* (YNB medium), intermediate *ex*
295 *vivo*, and large *ex vivo* cells, which may influence host cell recognition of *C. neoformans* cells.
296 Phagocytes such as platelets, neutrophils, and macrophages are critical for the
297 clearance of various pathogens. To identify those important for small cell clearance, we
298 systematically depleted each cell type and measured organ distribution of *ex vivo* populations
299 following tail vein injection. To address the role of macrophages, we depleted macrophages
300 from the liver, spleen, and bone marrow of mice with clodronate liposomes 48 hours prior to
301 inoculation (**Figures S3A and S3B**). Macrophage depletion reduced small *ex vivo* cell fungal
302 burden in the liver, while increasing fungal burden in the lungs, kidneys, and brain at 1 dpi
303 (**Figure 3E**). These results corroborate the findings of Sun *et al*, in that liver macrophages play
304 a critical role in filtering *C. neoformans* from the blood (Sun et al., 2019). However, we also
305 found that small *ex vivo* cells grow rapidly in the liver compared with *in vitro*-grown cells or other
306 *ex vivo* populations (**Figure 3F**), suggesting that attempts by the host to clear *C. neoformans*
307 cells by sequestering them in the liver may backfire.
308 Platelets can recognize either complement protein bound to microbes or microbial
309 features directly to initiate microbial clearance, especially in the spleen (Broadley et al., 2016).
310 Platelets don't appear to interact with encapsulated *C. neoformans*, or mediate the clearance of
311 *in vitro*-grown *C. neoformans* cells from the blood (Sun et al., 2019). When we depleted
312 platelets, we also did not see any effect on fungal dissemination (**Figures S4A-C**).
313 It is unclear whether neutrophils play a predominantly protective or detrimental role
314 during cryptococcosis, though there is evidence neutrophils can clear *C. neoformans* from the
315 blood (Sun et al., 2016; Zhang et al., 2016). Neutrophil depletion greatly increased fungal
316 burden in the lungs and brain when *in vitro*-grown fungal cells were injected intravenously (Sun
317 et al., 2016; Zhang et al., 2016). However, neutrophil-depletion prior to inoculation with small *ex*
318 *vivo* cells slightly increased lung fungal burden but did not affect fungal burden in other organs,
319 indicating that the small *ex vivo* cells are more resistant to neutrophil-mediated clearance than
320 typical *in vitro*-grown fungal cells (**Figures S4D-F**).
321
322 **Macrophage recognition of small *ex vivo* cells is partially mediated by mannose**
323 **exposure.**

324 We predicted that liver macrophages may recognize the high levels of exposed
325 mannose on the surface of small *ex vivo* cells. We isolated liver macrophages from healthy ~8-
326 week-old B6 mice (Li et al., 2014) and co-cultured them with 6 μm plastic beads, YNB-grown
327 cells, and sorted *ex vivo* populations at a multiplicity of infection of 2:1. Half of the wells also
328 received pretreatment with exogenous mannan, with the prediction that it would reduce
329 macrophage association if mannan recognition is critical. After 4 hours we washed away free
330 fungal cells, leaving only the fungal cells bound or internalized by macrophages, which we
331 define as "macrophage association".
332 Approximately 60% of macrophages had associated with 6 μm plastic beads by 4 hours,
333 indicating that the liver macrophages still displayed phagocytic capacity *ex vivo* (**Figure 3G**).
334 Additionally, 18% of liver macrophages associated with small *ex vivo* cells, which was more
335 than twice the frequency of intermediate and large *ex vivo* cells. Pretreatment with exogenous
336 mannan prior to infection reduced macrophage association with small *ex vivo* cells by ~40%, but
337 did not affect association with intermediate and large *ex vivo* cells, YNB-grown cells, or beads.
338 These data suggest that liver macrophages recognize small *ex vivo* cells in part through
339 exposed mannose, and that mannose exposure could contribute to fungal sequestration in the
340 liver.
341 Liver macrophages and other macrophages that sample the bloodstream are subject to
342 shear force, which can affect recognition and phagocytosis of microbes and other foreign matter
343 (Broadley et al., 2016). We assessed whether mannose exposure on small *ex vivo* cells affects
344 vascular clearance *in vivo* by intravenously injecting either 400 μg of exogenous mannan or
345 vehicle (PBS) 2-3 minutes prior to intravenous inoculation with 10^5 small *ex vivo* cells. 10
346 minutes later, we perfused mice to drive out non-recirculating fungal cells and plated organs for
347 colony forming units (CFUs) to estimate fungal burden. If mannose recognition contributed to
348 fungal clearance in a given organ, we expected to see reduced fungal burden in mice that
349 received exogenous mannan, compared with the vehicle control. We repeated this with different
350 fungal cell wall and capsule components (GXM, β-glucan, chitin), as well as polyinosinic acid
351 (poly(I)), which is a scavenger receptor ligand (Pearson et al., 1993).
352 Although mannan did reduce fungal clearance in the liver and kidneys by ~20% and in
353 the spleen by ~75% (**Figure 3H**), it was not the only fungal ligand that influenced vascular
354 clearance. Poly(I) reduced clearance to a strikingly similar extent as mannan. The purified
355 capsule polysaccharide GXM reduced clearance in the liver, spleen, kidneys at roughly the
356 same level (~40% reduction). β-glucan and chitin, on the other hand, did not appreciably affect
357 fungal clearance, possibly because of their buried position beneath the capsule. Fungal burden

358 in the brain was too low – usually less than 100 CFU per mouse - to detect changes. These
359 data indicate that clearance of small *ex vivo* cells is not dependent on a single cell surface
360 ligand and that there are tissue-specific dependencies on various fungal features that mediate
361 vascular clearance.
362

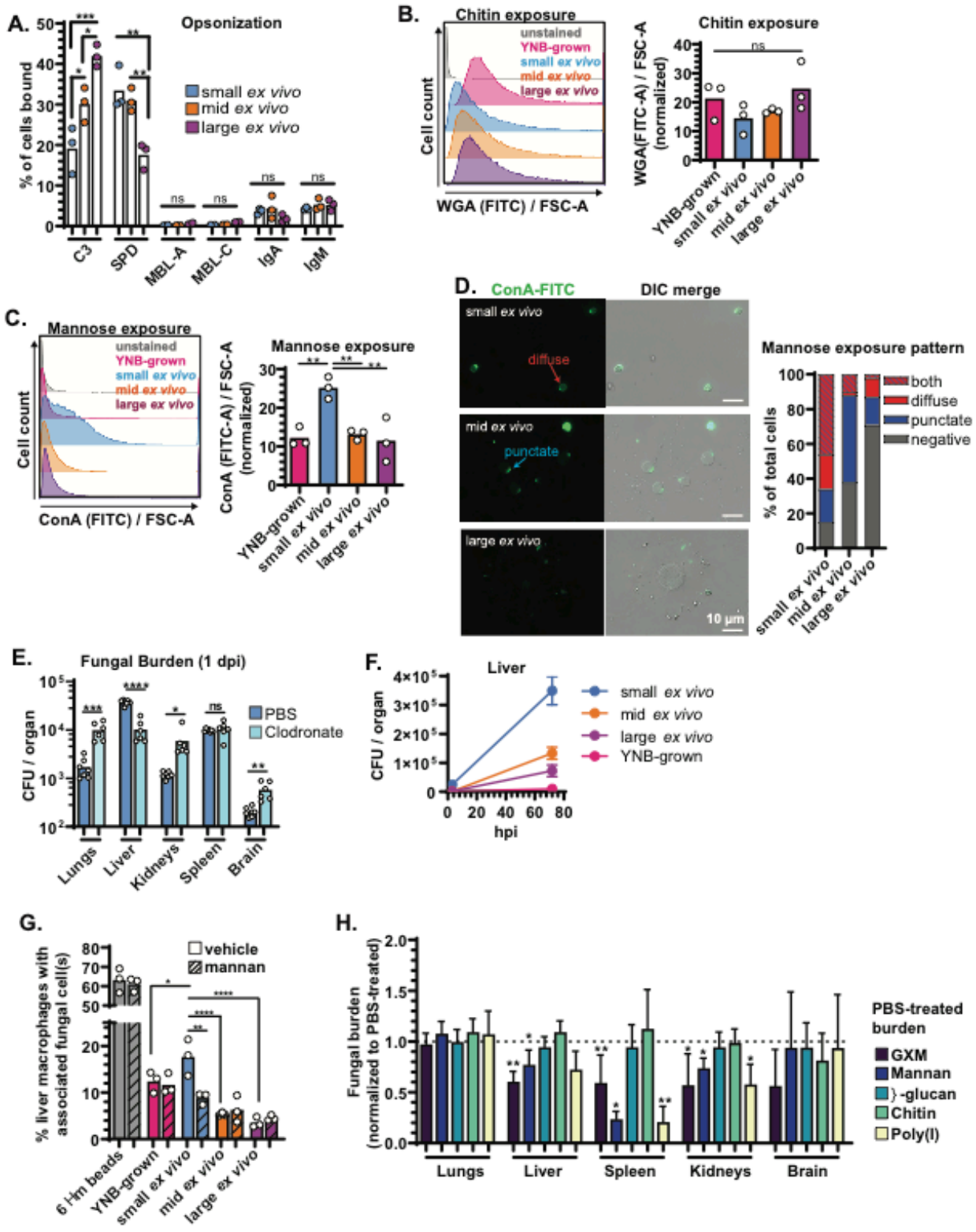
A.
Opsonization
% of cells bound
small ex vivo
mid ex vivo
large ex vivo
C3
SPD
MBL-A
MBL-C
IgA
IgM
B.
Chitin exposure
unstained
YNB-grown
small ex vivo
mid ex vivo
large ex vivo
Cell count
WGA (FITC) / FSC-A
Chitin exposure
WGA(FITC-A) / FSC-A (normalized)
C.
Mannose exposure
ConA (FITC) / FSC-A
ConA (FITC-A) / FSC-A (normalized)
D.
ConA-FITC
DIC merge
diffuse
punctate
10 µm
Mannose exposure pattern
both
diffuse
punctate
negative
% of total cells
E.
Fungal Burden (1 dpi)
CFU / organ
PBS
Clodronate
Lungs
Liver
Kidneys
Spleen
Brain
F.
Liver
CFU / organ
hpi
G.
vehicle
mannan
% liver macrophages with associated fungal cell(s)
6 µm beads
H.
Fungal burden (normalized to PBS-treated)
PBS-treated burden
GXM
Mannan
}-glucan
Chitin
Poly(I)

363

364

365 **Figure 3: Small *ex vivo* cells disseminate to extrapulmonary organs at a higher rate than**
366 **larger cells, with mannose recognition by macrophages contributing to their clearance**
367 **from the vasculature. (A)** Percentage of total cells bound by complement (C3), surfactant
368 protein D (SPD), mannose binding lectins A and C (MBL-A; MBL-C), IgA, and IgM. **(B)**
369 Representative flow plots and quantification of wheat-germ agglutinin (WGA) stained cells to
370 determine chitin exposure. **(C)** Representative flow plots and quantification of concanavalin A
371 (ConA) stained cells to determine mannose exposure. **(D)** Representative images and
372 characterization of mannose exposure pattern after staining with ConA (N=50 fungal cells). All
373 comparisons in Figure 2 were analyzed using one-way ANOVA and uncorrected Fisher's LSD
374 (ns: not significant; *p<0.05; **p<0.01; ***p<0.001; ****p<0.0001). All bar graphs display the
375 mean. **(E)** Fungal burden at 1 dpi in mice pretreated with either clodronate or vehicle control
376 (PBS) liposomes and then inoculated with small *ex vivo* cells and (Unpaired t test). **(F)** Fungal
377 burden in the livers of mice (N=4-6) inoculated with *ex vivo* fungal cells or fungal cells harvested
378 from minimal YNB (YNB) medium at 3 and 72 hpi. Points indicate the mean and the error bars
379 indicate standard deviation. **(G)** Percentage of primary cultured murine liver macrophages with
380 physically associated plastic beads or fungal cells (stained with Direct Yellow 96) after 4 hours.
381 Dashed lines indicate 10-minute pretreatment with exogenous mannan (One-way ANOVA and
382 uncorrected Fisher's LSD; N=2263-3197 total macrophages counted across 3 independent
383 replicates). **(H)** Fungal burden in mice intravenously treated with indicated ligand 2-3 minutes
384 prior to intravenous inoculation with small *ex vivo* fungal cells. Mice were perfused 10 minutes
385 post-inoculation and fungal burden was normalized to vehicle (PBS) treated controls (Unpaired
386 t-test; N=6 mice per group). All panels: ns: not significant *p<0.05; **p<0.01; ***p<0.001;
387 ****p<0.0001. All bar graphs display the mean.
388

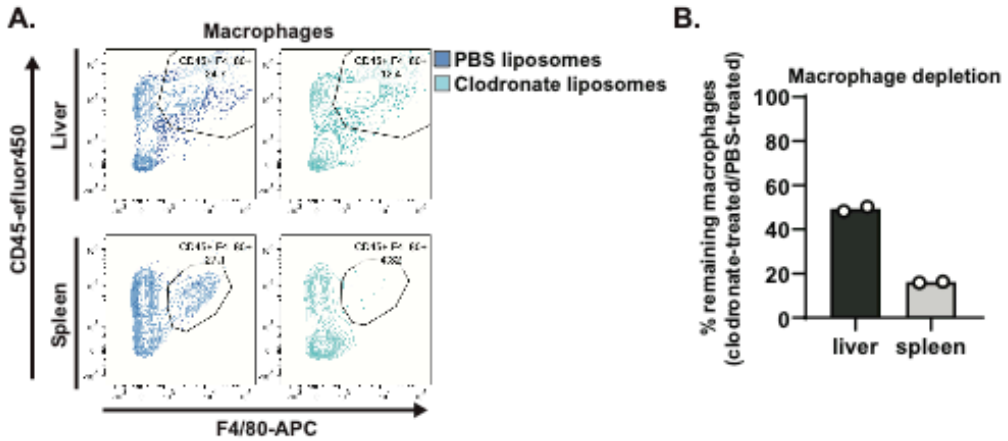

Supplemental Figure 3: Macrophage depletion efficiency in the liver and spleen. (A) Representative flow cytometry plots displaying the frequency of $CD45^+$, $F4/80^+$ macrophages in the liver and spleen after treatment with either PBS (control) liposomes or clodronate liposomes. **(B)** Quantification of macrophage depletion measured as the ratio of macrophages in clodronate-treated mice to PBS-treated mice.

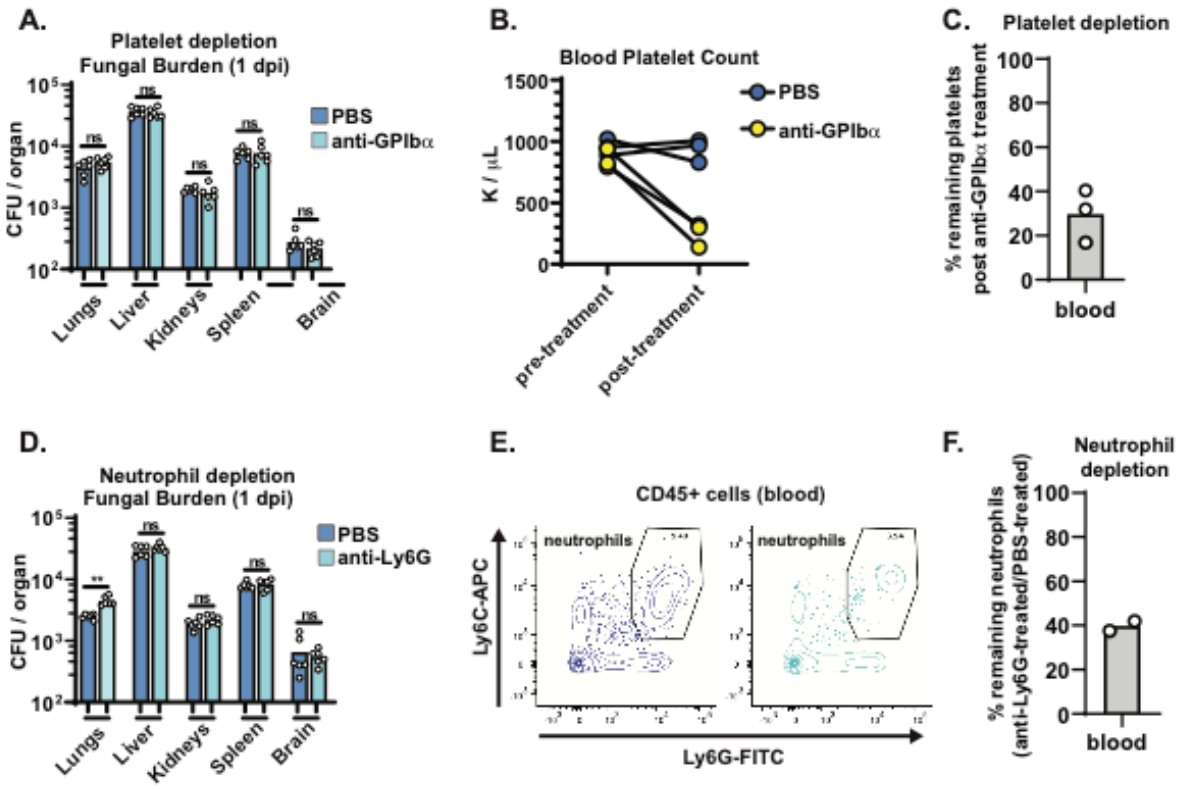

Supplemental Figure 4: Depletion of platelets or neutrophils does not affect the dissemination of small *ex vivo* cells. (A) Fungal burden in mice, measured by colony forming units (CFU), following treatment with PBS (control) or anti-GPIbα antibody to deplete platelets prior to intravenous inoculation with 10^5 small *ex vivo* cells / mouse. **(B)** Platelet count (K: units) in the blood before and after treatment with PBS (control) or anti-GPIbα antibody. **(C)** Quantification of platelet depletion in Figure S4B. **(D)** Fungal burden in mice treated with PBS (control) or anti-Ly6G antibody to deplete neutrophils prior to intravenous inoculation with 10^5 small *ex vivo* cells / mouse. **(E)** Representative flow cytometry plots displaying the frequency of $CD45^+$, $Ly6C^+$, $Ly6G^+$ neutrophils in the blood after treatment with either PBS (control) or anti-Ly6G antibody. **(F)** Quantification of neutrophil depletion measured as the ratio of neutrophils in anti-Ly6G antibody-treated mice to PBS-treated mice. All comparisons in Figure S4 were analyzed using unpaired t-tests (ns: not significant *p<0.05; **p<0.01; ***p<0.001; ****p<0.0001). All bar graphs display the mean.

411 **Enhanced small *ex vivo* cell dissemination is not solely dependent on size.**

412 We next assessed whether small *ex vivo* cells disseminate more efficiently due to their
413 size alone, or if there were other contributing factors. We inoculated mice via the tail vein with
414 either large *ex vivo* cells, small *ex vivo* cells or size-matched inert polystyrene beads. Large *ex*
415 *vivo* cells disseminated similarly to size-matched 25 μm beads; the majority resided in the lungs
416 at 3 hpi (**Figure 4A**). Additionally, more 6 μm beads traveled past the lungs to reach the liver
417 and spleen compared to 25 μm beads. However, small *ex vivo* cells reached the liver and
418 spleen at an even higher frequency, indicating that absolute size influences fungal
419 dissemination through the vasculature, but it is not the only contributing factor.

420 We next examined *in vitro* conditions that could reproduce the small *ex vivo* cell
421 morphotype and dissemination profile. Previously, we observed that cells grown in capsule-
422 inducing medium (CAP; 10% Sabouraud's dextrose broth buffered to pH 7.4) shifted toward
423 smaller cell and capsule size if they were supplemented with conditioned medium (CM) from
424 cells grown in non-capsule inducing medium (YNB) after 24 hours (Denham et al., 2018). YNB
425 medium contains vitamins, nitrogen, and glucose but not amino acids. YNB-grown cells
426 suppress capsule formation, and are typically <10 μm in diameter. CAP medium induces
427 capsule formation and is sufficient for cell division. We collected CM by filtering the supernatant
428 from saturated YNB-grown cultures. In this case, CM consists of unspent nutrients and soluble
429 fungal factors secreted during growth in non-capsule inducing conditions.

430 We compared the dissemination profile of small *ex vivo* cells to cells grown in three *in*
431 *vitro* populations: (1) YNB-grown cells (2) CAP-grown cells, and (3) CAP-grown cells
432 supplemented with CM (CAP+CM). We also subjected the *in vitro*-grown populations to the
433 same sorting process as *ex vivo* cells by sorting YNB, and CAP+CM-grown cells from the
434 "small" FSC-A gate (YNB cells: 5.6 μm median total diameter; CAP+CM cells: 6.5 μm median
435 total diameter; few YNB or CAP+CM cells fell in the "mid" or "large" FSC-A gates) and sorting
436 the CAP-grown cells from the "mid" FSC-A gate (12.1 μm median total diameter; few CAP-
437 grown cells fell into the "small" or "large" FSC-A gates) (**Figure 4B**).

438 Culture conditions and morphology of cells in the inoculum heavily impacted
439 dissemination. Only CAP+CM cells replicated the dissemination profile of small *ex vivo* cells in
440 terms of fungal burden at 3 hours and 3 days post-inoculation (**Figure 4C**). Despite being
441 roughly the same size as small *ex vivo* cells, YNB-grown cells displayed similar fungal burden to
442 CAP-grown cells at 3 hours, and lower fungal burden in extrapulmonary organs than CAP,
443 CAP+CM, and small *ex vivo* cells at 3 days. Therefore, both absolute fungal cell size, and the
444 physiological state of cells entering the blood influence the outcome of vascular dissemination.

445

446 **Host-adapted cells survive better in the blood than cells grown in nutrient-replete**
447 **medium.**

448 The caveat to using fungal burden as a readout for dissemination is that we cannot
449 easily distinguish between the ability of cells to reach certain organs and their ability to survive
450 in those organs. We hypothesized that YNB-grown cells may not be as primed for survival in the
451 bloodstream as cells sorted from infected host-tissue or cells grown under capsule-inducing
452 medium (CAP medium).

453 To address that hypothesis, we examined the survival of *in vitro*- and *ex vivo*-sorted cells
454 in whole mouse blood or liver macrophage co-culture (multiplicity of infection of 1:1). We used
455 DMEM as a tissue culture medium control (96-well plates, 37 °C, 5% CO_2, static). We assessed
456 fungal cell survival as a percentage of input at 0-, 24-, and 48-hour timepoints. Liver
457 macrophages suppressed *in vitro* and *ex vivo* cell growth equivalently (**Figures 4D and 4E**).
458 However, the *ex vivo* populations and *in vitro* populations from host-like conditions survived
459 better in blood than YNB-grown cells (**Figure 4F and 4G**), with large and intermediate *ex vivo*
460 populations faring the best. These results support the idea that size and physiology are critical
461 for bloodstream dissemination: small *ex vivo* cells potentially combine the stress resistance
462 required for increased survival in the blood with the smaller cell size required for widespread
463 dissemination via microcapillaries.

464

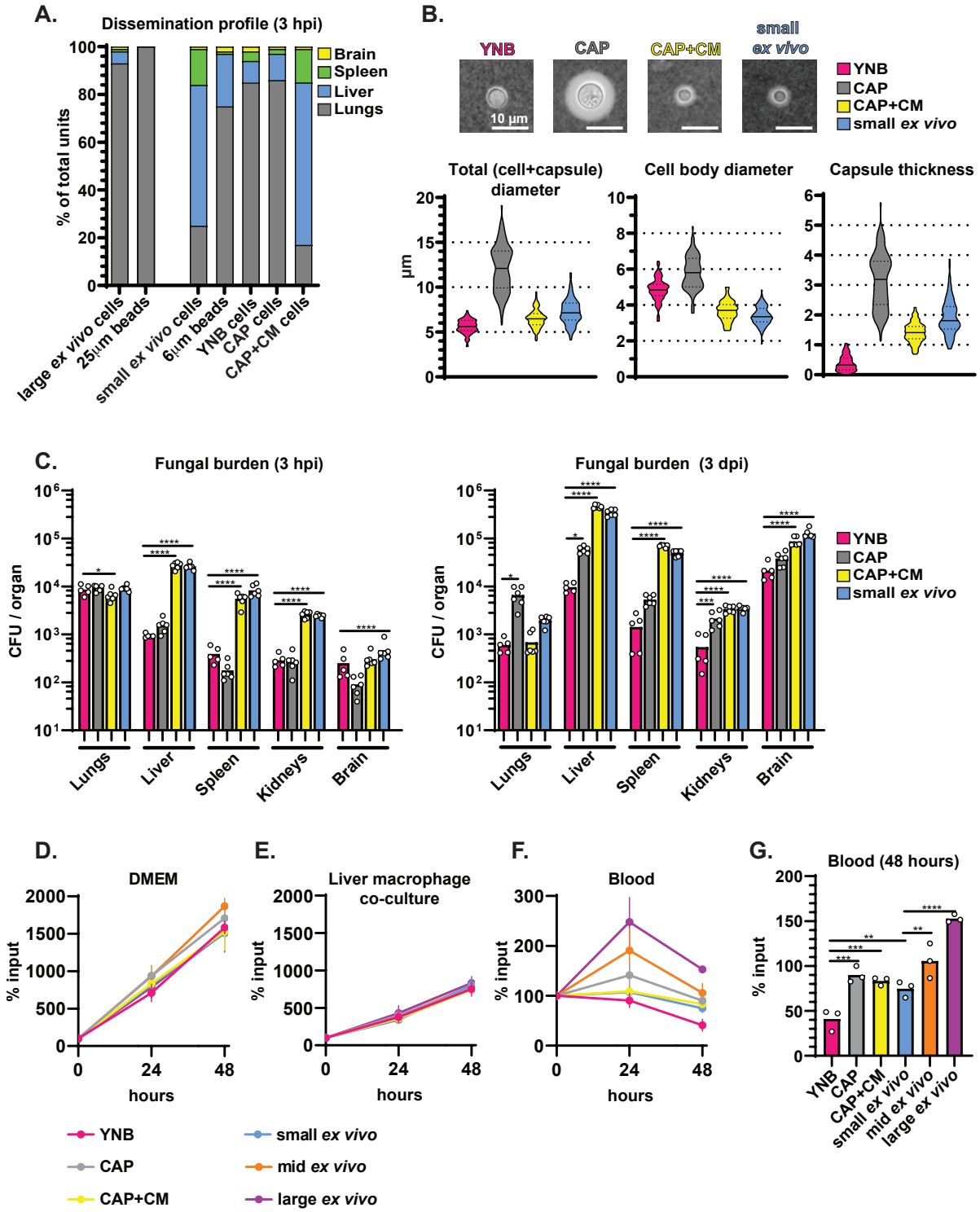

Figure 4: Small cells generated under host-like conditions *in vitro* replicate the dissemination profile of small *ex vivo* cells. (A) Percentage of total plastic beads or live cells

468 in the indicated organ 3 hours post-intravenous inoculation (hpi). **(B)** Representative India ink
469 images and quantification of cell and capsule size (N=100 fungal cells). YNB (minimal YNB
470 medium); CAP (capsule inducing medium); CAP+CM (capsule inducing medium supplemented
471 with 10% conditioned medium). **(C)** Fungal burden, measured by colony forming units (CFU), in
472 mice at 3 hpi. and 3 days post-inoculation (dpi). **(D)** Fungal cell survival in Dulbecco's modified
473 Eagle's medium (DMEM) and **(E)** liver macrophage co-culture (multiplicity of infection of 1:1)
474 measured as a percentage of input. **(F)** Fungal cell survival in mouse blood measured as a
475 percentage of input over 48 hours and **(G)** at 48 hours growth. All comparisons in Figure 4 were
476 analyzed using one-way ANOVA and uncorrected Fisher's LSD (*$p<0.05$; **$p<0.01$; ***$p<0.001$;
477 ****$p<0.0001$). All bar graphs display the mean.
478

479 **Expression of phosphate acquisition genes differ between small cells and larger *C.***
480 ***neoformans* cells.**
481 Since CAP+CM-grown cells resemble small *ex vivo* cells in terms of cell + capsule size
482 and vascular dissemination, we hypothesized that they might suitably model small cell formation
483 in the lungs. We analyzed the transcriptome of cells grown in YNB, CAP, and CAP+CM medium
484 to identify genes that might facilitate the transition to small cell size in host-like capsule inducing
485 conditions. We also analyzed the transcriptome of small, intermediate and large *ex vivo* cells.
486 Comparing the transcriptome of CAP, CAP+CM, and the *ex vivo* populations to YNB-
487 grown cells demonstrated that the YNB-grown transcriptome is vastly different from each of
488 these populations (**Figure 5A** and **5B**). There were also 1085 up-regulated and 1297
489 downregulated genes shared only among the *ex vivo* populations relative to YNB-grown cells.
490 Core sets of 699 and 291 genes were up- and down-regulated respectively among the *ex vivo*
491 populations and CAP/CAP+CM populations relative to YNB-grown cells, demonstrating that the
492 transcriptome within the host environment is quite distinct from *in vitro* conditions that induce
493 virulence traits. Among the *ex vivo* populations, small *ex vivo* cells were the most
494 transcriptionally distinct (**Figure 5A**). 928 genes were differentially expressed in small vs
495 intermediate *ex vivo* cells, and 2,365 genes were differentially expressed in small vs large *ex*
496 *vivo* cells. For comparison, only 93 genes were differentially expressed in intermediate vs large
497 *ex vivo* cells (**Figure 5A**).
498 Gene ontology term (GO-term) enrichment analysis revealed that phosphate ion
499 transport was upregulated in CAP-grown cells vs YNB-grown cells (**Figure 5C**), and
500 downregulated in CAP+CM vs CAP-grown cells (**Figure 5D**). In other words, phosphate
501 acquisition genes are induced when cells enter capsule-inducing conditions (CAP medium), and
502 then suppressed following supplementation with CM.
503 We observed the same trends when analyzing the expression of specific genes involved
504 in phosphate acquisition and storage (**Figure 5E**). When *C. neoformans* cells are starved of
505 phosphate, the phosphate acquisition transcription factor, Pho4, translocates to the nucleus
506 where it promotes its own gene expression and the expression of genes involved in phosphate
507 acquisition and storage. These include phosphate transporters: *PHO84*, *PHO89*, and *PHO840*;
508 phosphatases: *APH1* (secreted/vacuolar acid phosphatase) and *APH4* (predicted intracellular
509 acid phosphatase); and *VTC4* (vacuolar transport chaperone involved in processing
510 polyphosphate). Pho4-dependent genes were upregulated in CAP vs YNB-grown cells and then
511 suppressed in following CM supplementation—although many phosphate acquisition genes still
512 remained more highly expressed in CAP+CM-grown cells compared with YNB-grown cells.

Figure 5

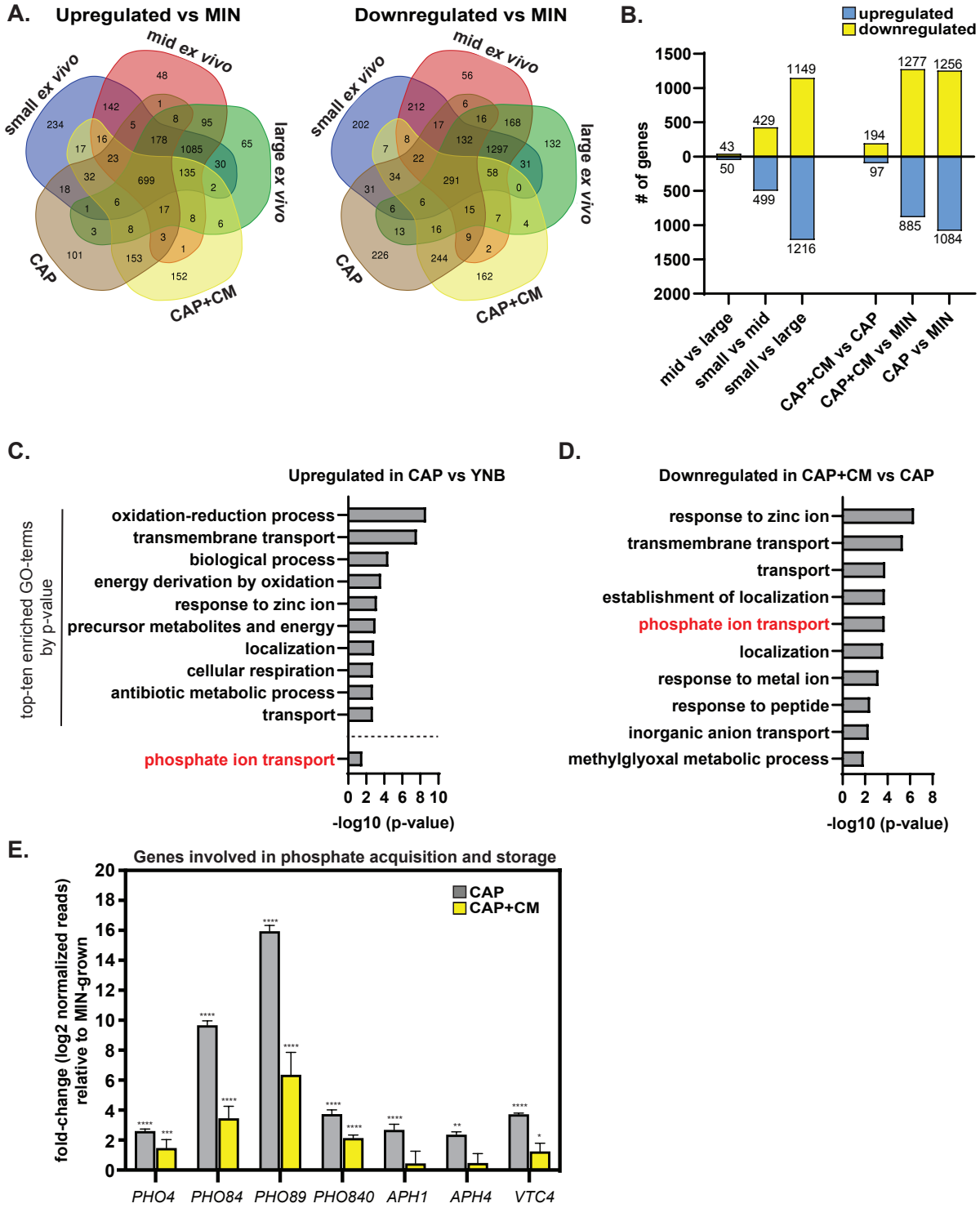

Figure 5: Expression of phosphate acquisition genes correlate with cell and capsule size changes *in vitro* and are upregulated *in vivo*. (A) Venn diagram of genes upregulated or

516 downregulated in different conditions relative to YNB-grown cells (YNB: minimal YNB medium;
517 CAP: capsule-inducing medium; CAP+CM: capsule inducing medium supplemented with 10%
518 conditioned medium). **(B)** Comparisons of the total number of differentially regulated genes
519 among *in vitro*-grown populations. **(C)** Top-ten most significantly enriched gene ontology (GO)
520 terms representing genes upregulated in CAP vs YNB-grown cells (-log10 (p-value)). Phosphate
521 ion transport was #46. **(D)** Top-ten most significantly enriched GO-terms representing genes
522 downregulated in CAP+CM vs CAP-grown cells (-log10 (p-value)). **(E)** Select phosphate
523 acquisition and storage RNA-seq gene expression relative to YNB-grown cells (adjusted p
524 values; *$p<0.05$; **$p<0.01$; ***$p<0.001$; ****$p<0.0001$). All bar graphs display the mean and error
525 bars the standard deviation.
526

527 **Phosphate drives *C. neoformans* populations toward smaller morphotypes**

528 We hypothesized that phosphate might be a critical nutrient that facilitates the
529 emergence of small cells in CAP+CM media. Conditioned medium consists of unspent YNB
530 medium and soluble fungal cell derived factors (Albuquerque et al., 2013). YNB medium is
531 defined, so we screened every component individually (including phosphate) to determine which
532 components are sufficient to induce small cell formation when cells are grown in CAP medium.
533 We also tested two soluble fungal-derived factors that accumulate during growth in YNB
534 medium: exo-GXM (Denham et al., 2018) and the quorum sensing-like peptide Qsp1 (Homer et
535 al., 2016; Lee et al., 2007).

536 We grew cells for 24 hours in YNB medium, then sub-cultured 10^5 cells/mL into CAP
537 medium for another 24 hours. We then sub-cultured CAP-grown cells 1:1 into fresh CAP
538 medium with 10% of the final volume being a YNB medium component, fungal-derived factor, or
539 water as the vehicle control. After a final 24-hour period, we measured cell size (FSC-A) by flow
540 cytometry.

541 Conditioned YNB medium and fresh YNB medium were sufficient to stimulate a shift
542 toward smaller cell size (**Figures 6A and 6B**). Among the YNB medium components, only
543 phosphate was sufficient to stimulate a shift toward smaller cell size (**Figure S5A**), and did so in
544 a concentration-dependent manner (**Figures 6A and 6B**). Phosphate-supplemented cells
545 decreased both total (cell+capsule) diameter (**Figure 6C**) as well as cell (**Figure S6A**) and
546 capsule (**Figure S6B**) size individually. Phosphate was also sufficient to induce a shift toward
547 smaller size for cells grown in titan cell-inducing medium (5% Sabouraud's, 10% fetal calf
548 serum, 15 μM sodium azide, pH 7.4, 5% CO_2, 37 °C) (**Figure S5B**).

549 We previously reported that exo-GXM may trigger the formation of smaller cells
550 (Denham et al., 2018). However, we were unable to reproduce those results (**Figure S5A**),
551 possibly due to differences in exo-GXM preparation, but more likely because we previously
552 solubilized exo-GXM in phosphate buffered saline. Qsp1 is a cell-density dependent signaling
553 peptide that suppresses the formation of titan cells (Trevijano-Contador et al., 2018). However,
554 the addition of Qsp1 did not affect cell size in this model (**Figures S5A and S5B**).

555 The Pho84 and Pho840 phosphate transporters are phosphate/H^+ symporters, and *C.*
556 *neoformans* therefore requires a proton gradient to efficiently transport phosphate into the cell
557 (Kretschmer et al., 2014). In alkaline pH, *C. neoformans* struggles to efficiently import
558 phosphate and upregulates phosphate acquisition machinery (Kretschmer et al., 2014; Lev et
559 al., 2017). *C. neoformans* releases metabolites that acidify the local microenvironment and
560 increase nutrient uptake (Himmelreich et al., 2003; Wright et al., 2002). For instance,

561 cryptococcomas in the brain acidify to levels as low as pH 5.5 (Himmelreich et al., 2003; Wright
562 et al., 2002).
563 We measured lung pH in mice inoculated with *C. neoformans* throughout infection, and
564 found that pH in the lungs decreased from ~7.4 to as low as ~6.3 between 3 and 17 dpi (**Figure**
565 **6D**). Phosphate did not induce significant shifts in FSC-A-measured cell size when CAP
566 medium was buffered to 6.3, potentially because phosphate availability in CAP medium buffered
567 to pH 6.3 is not as limiting as pH 7.4 (**Figures 6A and 6B**). However, we did measure a modest,
568 but significant decrease in total (cell+capsule) diameter by light microscopy when pH 6.3 CAP-
569 grown cells were supplemented with phosphate (**Figure 6C**), which was mostly due to a
570 decrease in capsule thickness (**Figure S5**). When phosphate availability suddenly increases
571 due to higher extracellular concentrations, *C. neoformans* cells shift toward smaller
572 morphotypes.
573
574 **Limiting phosphate acquisition genetically suppresses morphogenesis *in vivo***
575 Since phosphate was sufficient to trigger cell and capsule size reduction *in vitro*, we
576 hypothesized that limiting phosphate acquisition *in vivo* would alter morphogenesis, perhaps
577 delaying the appearance of small morphotypes. To test this hypothesis, we intranasally
578 inoculated mice with wild-type KN99, or either of two independently constructed KN99:*pho4*Δ
579 strains, which lack the gene encoding the transcription factor *pho4*. Without *pho4*, *C.*
580 *neoformans* cells fail to adequately upregulate genes involved in phosphate acquisition when
581 available phosphate is limiting, and become hypersensitive to alkaline conditions. The *pho4*Δ
582 mutant is attenuated for growth in the lungs but more severely attenuated for dissemination to
583 the brain, due to its poor survivability in alkaline blood (Lev et al., 2017). Our findings replicated
584 the work from Lev *et al.*, in that the *pho4*Δ mutant cells were attenuated for proliferation in the
585 lungs **(Figure 6E)** and dissemination to the brain **(Figure 6F)**. We also found that cell and
586 capsule size of *pho4*Δ mutant cells populating the lungs was static and less heterogeneous
587 relative to wild-type cells **(Figures 6G, S5D-F)**. Most *pho4*Δ mutant cells remained between 10
588 and 20 μm in total (cell + capsule) diameter over 17 days **(Figure 6G)**, with many of them also
589 exhibiting irregular budding **(Figure S5F)**. Total median wild-type cell + capsule diameter was
590 far larger than the *pho4*Δ cells at day 3 (wild-type: 26 μm; *pho4*Δ #1: 15 μm; *pho4*Δ #2: 14 μm)
591 and smaller than the *pho4*Δ cells at day 17 (wild-type: 10 μm; *pho4*Δ #1: 14 μm; *pho4*Δ #2: 15
592 μm). *pho4*Δ cells therefore appear to be deficient in titan cell formation *in vivo* (**Figure 6G**).
593 However, this result potentially obscures whether *pho4*Δ mutant cells are able to form small
594 cells.

595 In our *in vitro* small cell induction system, titan cell formation is not required. To eliminate
596 the possibility that *pho4*Δ cells cannot form small cells because they cannot form titan cells, we
597 induced small cells with either conditioned medium or inorganic phosphate. At pH 7.4, *pho4*Δ
598 cells exhibit constitutively small cell bodies and capsules. *pho4*Δ cells do not get substantially
599 smaller in response to phosphate or conditioned medium (**Figure 6H**). At pH 6.8, the upper pH
600 range in the lungs at 10 dpi (**Figure 6D**), we found that *pho4*Δ cells' total diameters were only
601 slightly smaller than wild-type cells at pH 6.8 (wild-type: 10.6 μm, *pho4*Δ #1: 9 μm; *pho4*Δ #2: 9
602 μm), while the difference was more dramatic at pH 7.4 (wild-type: 10.2 μm, *pho4*Δ #1: 7.3 μm;
603 *pho4*Δ #2: 7.5 μm) (**Figure 6I**). At pH 6.8, both wild-type and *pho4*Δ cells became smaller in
604 response to conditioned medium but not phosphate, while pH 7.4-grown *pho4*Δ did not exhibit a
605 cell size shift in response to either conditioned medium or phosphate (**Figure 6H**). Together,
606 these data demonstrate that *PHO4* is necessary for phosphate-induced small cell formation at
607 pH 7.4 and that this phosphate-induced pathway could well be the only molecular trigger of
608 seed cell formation at pH 7.4. Our observation that *pho4*Δ cells' inability to form small cells at pH
609 7.4 is suppressed at pH 6.8 could indicate that two pathways exist to drive small cell formation.
610 However, since *pho4*Δ cells' growth defects are suppressed at acidic pH (Lev et al., 2017),
611 Pho4's transcriptional repertoire and therefore *pho4*Δ cells' inability to form small cells could
612 also be suppressed.
613 Finally, we measured phosphate levels within *C. neoformans* cells during growth under
614 capsule-inducing conditions (10% Sabouraud's pH 7.4 or pH 6.8) and following *in vitro* induction
615 of small cells. We found that small cells contained a higher concentration of phosphate on a per
616 cell basis, despite their smaller cell volume (**Fig. S5G**). Small cell formation therefore involves
617 increased acquisition of a limiting nutrient and is triggered by multiple common signals, strongly
618 supporting the idea that it is a major pathway that can be activated under a variety of conditions.
619

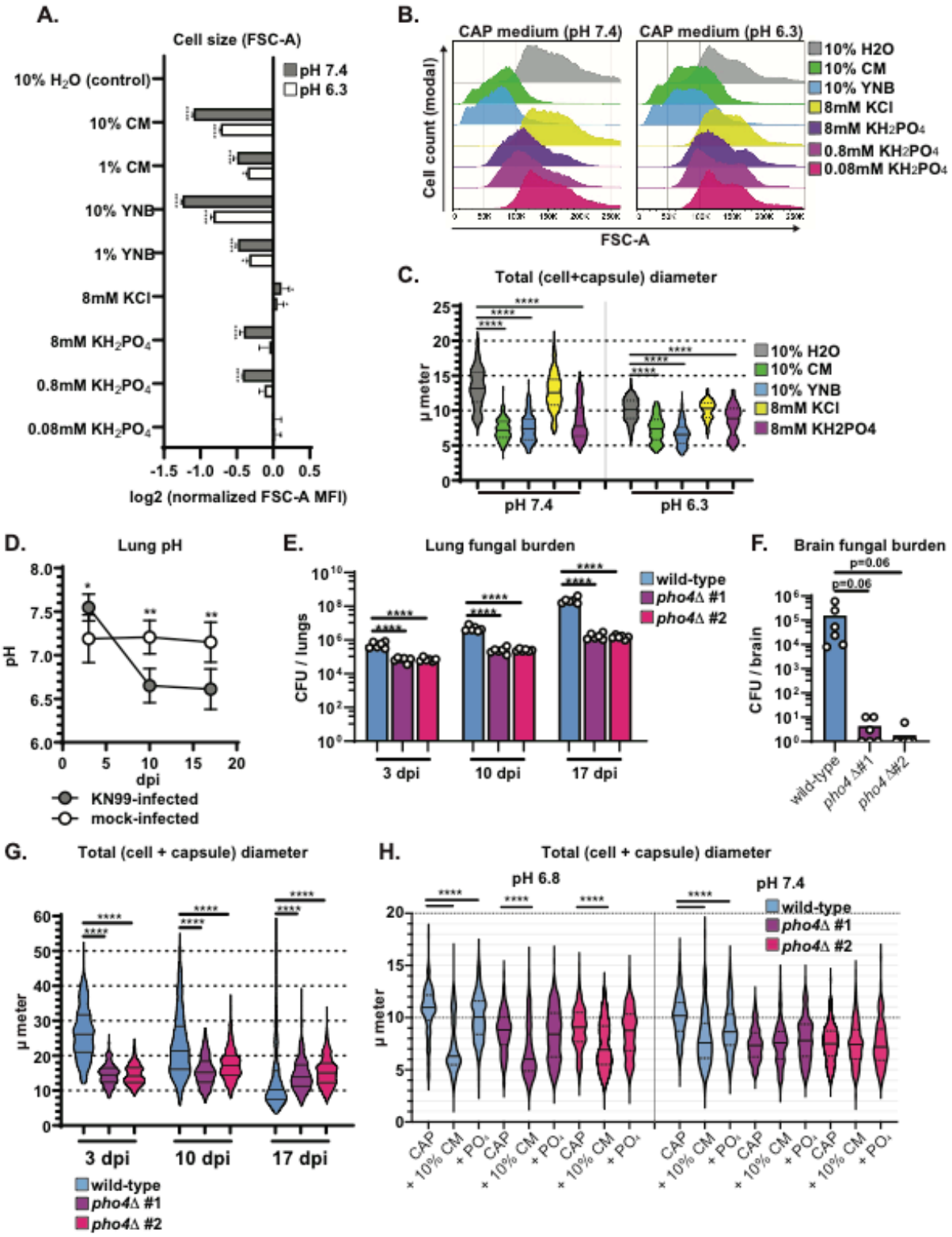

Figure 6: Phosphate is sufficient to drive *C. neoformans* toward smaller morphotypes in alkaline host-like conditions and is required for morphogenesis *in vivo*. (A) Cell size

623 measured using flow cytometry forward scatter (FSC-A) after growth in CAP-medium (10%
624 Sabouraud's pH 7.4) and supplementation with the indicated factor (YNB: minimal YNB
625 medium; CAP: capsule-inducing medium; CAP+CM: capsule inducing medium supplemented
626 with 10% conditioned medium). FSC-A median fluorescence intensity (MFI) was normalized to
627 control (10% H_2O)-treated cells (one-way ANOVA and uncorrected Fisher's LSD). Bar graphs
628 display the mean. **(B)** Representative flow cytometry plots for conditions in Figure 6A. **(C)** Total
629 (cell + capsule) diameter measurements representing conditions in Figure 6A (Mann-Whitney U-
630 test; N=200 fungal cells). Solid lines in the violin plots indicate the median and dotted lines mark
631 quartiles. **(D)** pH in *C. neoformans* strain KN99-infected and mock-infected mouse lungs at 3,
632 10, and 17 days post-inoculation (dpi) (N=4 mice; one-way ANOVA and uncorrected Fisher's
633 LSD; error bars represent standard deviation). **(E)** Lung fungal burden in mice at 3, 10, and 17
634 dpi (One-way ANOVA and uncorrected Fisher's LSD). The bar graph represents the mean. **(F)**
635 Brain fungal burden in mice at 17 dpi (One-way ANOVA and uncorrected Fisher's LSD). The bar
636 graph represents the mean. **(G)** Total diameter (cell + capsule) measurements at 3, 10, and 17
637 dpi of mice (Mann-Whitney U test; N=6 mice per timepoint; 50, 100, and 150 wild-type cells
638 measured per mouse at days 3, 10, and 17 respectively. 50, 50, and 100 *pho4*Δ mutant cells
639 measured per mouse at days 3, 10, and 17 respectively) **(H)** Total (cell + capsule) diameter
640 measurements of wild-type and *pho4*Δ mutant cells after growth in CAP-medium (10%
641 Sabouraud's at labeled pH, "control") and supplementation with the indicated factor (10%
642 conditioned medium or 800 μM PO_4 at **(H)** pH 7.4 or **(I)** pH 6.8 (Mann-Whitney test; N = 3
643 biological replicates per experiment and >100 cells measured per replicate. The solid line
644 represents the population median and the dotted lines the 25th and 75th percentiles.). All
645 comparisons marked as significant represent populations for which the 95% confidence interval
646 does not overlap. All panels: ns: not significant *p<0.05; **p<0.01; ***p<0.001; ****p<0.0001.
647

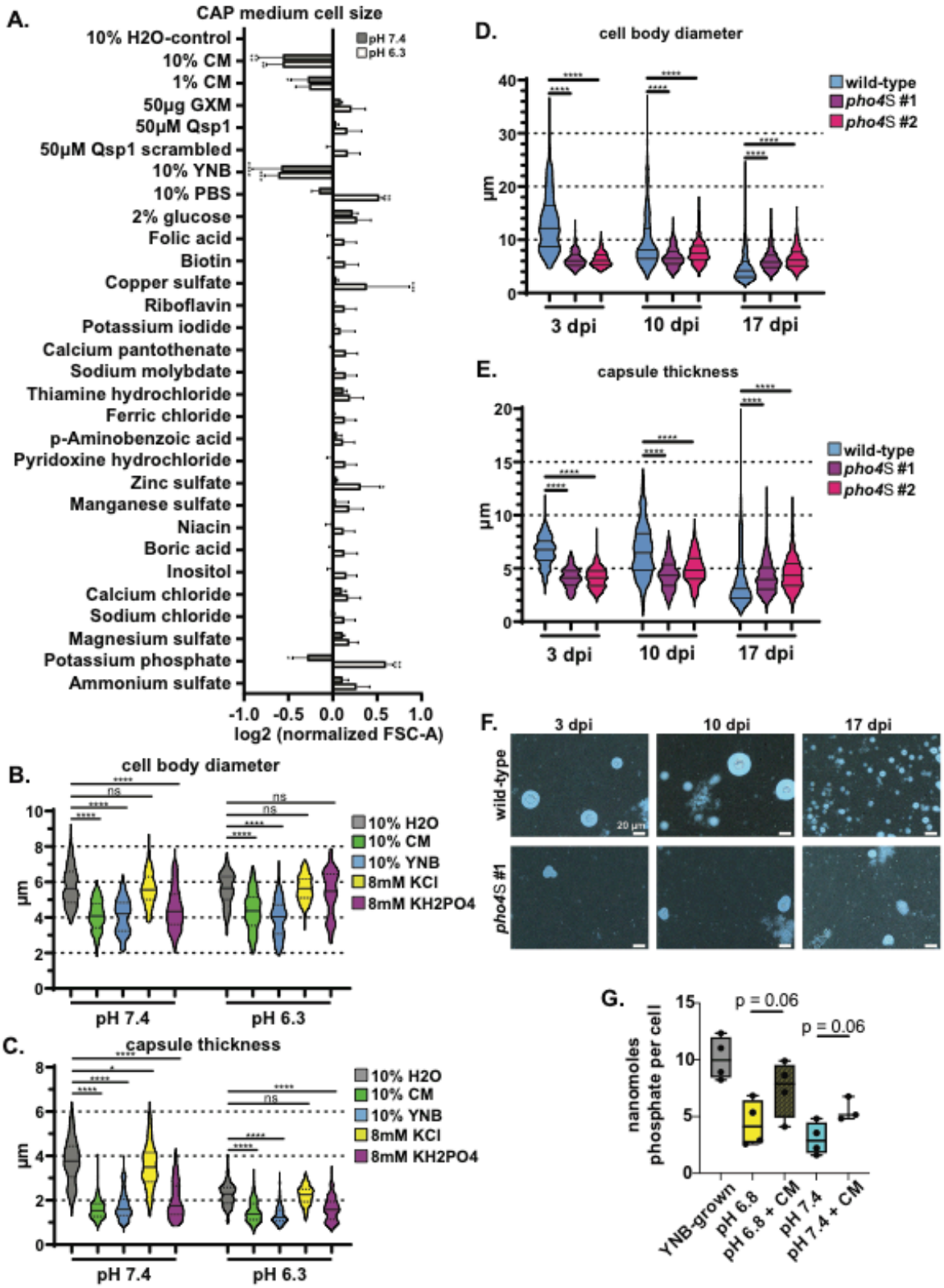

Supplemental Figure 5: Screen for factors that induce cell size reduction. (A) Fungal cell size measured by forward scatter-area (FSC-A). Cells were cultured in capsule inducing

651 medium (CAP medium) buffered to pH 7.4 or 6.3 before subculture (1:1) in fresh medium with
652 10% of the final volume being the indicated supplement solubilized in H_2O (CM: conditioned
653 medium; GXM: glucuronoxylomannan; YNB: minimal YNB medium; PBS: phosphate buffered
654 saline). Comparisons in Figure S5A were analyzed using one-way ANOVA and uncorrected
655 Fisher's LSD (ns: not significant; *p<0.05; **p<0.01; ***p<0.001; ****p<0.0001). All bar graphs
656 display the mean and error bars indicate standard deviation. **(B)** Cell body diameter and **(C)**
657 capsule thickness of cells cultured in capsule inducing medium (CAP medium) buffered to pH
658 7.4 or 6.3 before subculture (1:1) in fresh medium with 10% of the final volume being the
659 indicated supplement solubilized in H_2O (CM: conditioned medium; YNB: minimal YNB
660 medium). **(D)** Cell body diameter and **(E)** capsule thickness measurements at 3, 10, and 17
661 days post-intranasal inoculation (dpi) of mice (Mann-Whitney U test; N=6 mice per timepoint;
662 50, 100, and 150 wild-type cells measured per mouse at days 3, 10, and 17 respectively. 50, 50,
663 and 100 *pho4*Δ mutant cells measured per mouse at days 3, 10, and 17 respectively). Solid
664 lines in the violin plots indicate the median and dotted lines mark quartiles. All comparisons in
665 Figure S5B-E were analyzed using Mann-Whitney U-tests; N=200 fungal cells (ns: not
666 significant; *p<0.05; **p<0.01; ***p<0.001; ****p<0.0001). **(F)** Representative India ink images of
667 fungal cells quantified in Fig. 6G. Scale bars represent 20 μm. **(G)** Nanomoles of phosphate
668 cells grown in YNB, CAP-medium (pH 6.8 or pH 7.4)
669

670 **Components of *C. neoformans*'s environmental niche induce the small cell morphotype**

671 Phosphate is potentially available from a number of sources that *C. neoformans* could
672 encounter either in the environment or during infection. These include nucleotide pools within
673 both fungal cells and mammalian tissues and cells (Beis and Newsholme, 1975; Harris et al.,
674 1958) and phosphate in the blood at concentrations in the millimolar range (Beis and
675 Newsholme, 1975). Moreover, the infection process itself could increase the amount of
676 extracellular phosphate within host tissues. Neutrophil extracellular traps (NETs) include
677 extruded neutrophil DNA (Brinkmann et al., 2004). Cell lysis releases intracellular nucleoside
678 mono-, di-, or triphosphates, with ATP in particular acting as a signal of damage (Grygorczyk et
679 al., 2021). Extracellular ATP is released by host cells during inflammation (Dosch et al., 2018),
680 in response to injury (Gault et al., 2014), by macrophages in response to bacterial infection (Ren
681 et al., 2014), and as an apoptotic signal (Elliott et al., 2009). Outside the host, *C. neoformans* is
682 often found in association with pigeon nests and guano (Emmons, 1955). Bird guanos are rich
683 in phosphate (Otero et al., 2018). Nucleotide sugars are precursors for critical fungal cell wall
684 components. UDP-GlcNAc is polymerized into chitin (Gow et al., 2017). UDP-glucose is
685 important for β-glucan (Agustinho et al., 2018) and GXM synthesis (Agustinho et al., 2018;
686 Chung and Brown, 2020). However, GXM is synthesized in the secretory compartments
687 (Yoneda and Doering, 2006), so it is possible that exogenous UDP-sugars are not incorporated
688 into GXM or GXMGal because of the challenges of transporting them from the extracellular
689 space to the ER and Golgi (Agustinho et al., 2018). β-glucan and chitin are synthesized at the
690 plasma membrane, so extracellular precursors could be directly incorporated into these
691 structures.

692 Phosphate availability also varies widely with pH. In the soil environment, phosphate is
693 bound by calcium at alkaline pH and aluminum, iron, and manganese at acidic pHs (Becquer et
694 al., 2014; Hasan et al., 2016). In the host, pH is tightly controlled, but certain conditions,
695 including lung infections, cause respiratory acidosis and decrease the local pH (André et al.,
696 2022). We observe such a pH decrease in the lungs of *C. neoformans*-infected mice (**Fig. 6D**).

697 Using our *in vitro* small cell induction protocol, we tested whether or not a variety of
698 different phosphate sources could trigger small cell formation. *E. coli* genomic DNA and sheared
699 salmon sperm DNA (ssDNA) were both able to induce a modest but significant shift in the
700 median total diameter of the *C. neoformans* population, from 9.4 microns (at pH 7.4) to 8.0
701 microns for *E. coli* genomic DNA and 8.3 microns for ssDNA (**Fig. 7A**). Of the nucleoside
702 mono-, di-, and triphosphates, nucleoside triphosphates (NTPs) induced the greatest reduction
703 in median population diameter at both pH 6.8 (8.4 to 7.1 microns) and pH 7.4 (9.4 microns to

704 6.7 microns) (**Fig. 7B,C**). This appears to be a synergistic effect of multiple NTPs, as the
705 median diameter shift induced by all four NTPs together was greater than any individual NTP
706 (**Fig. S6A,B**). Among the nucleotide sugars, UDP-GlcNAc, a precursor for chitin, induced the
707 largest shift in the median population diameter at both pH 6.8 and pH 7.4 (**Fig 7D**), from 8.9
708 microns to 7.4 microns at pH 7.4 and 9.3 microns to 7.0 microns at pH 6.8. UDP-glucuronic
709 acid, a GXM precursor, induced a significant shift in median diameter as well.
710 However, the largest shift in cell size we observed was in response to pigeon guano
711 (**Fig. 7E, Fig. S6C,D**), which surpassed even conditioned medium as an inducing agent. The
712 median total diameter in CAP at pH 6.8 was reduced from 9.9 microns to 4.4 microns with
713 exposure to 10% guano medium. At pH 7.4, guano medium induced a shift in median total
714 diameter from 10.1 microns to 4.3 microns. Since volume is a function of the radius cubed ($V =$
715 $4/3 \times \pi \times r^3$) and radius = ½ x diameter, the volume of capsule-induced cells is 11-fold greater
716 than the volume of a guano-induced small cell. Even relatively modest reductions in diameter,
717 such as that induced by UDP-GlcNAc at pH 7.4, represents an almost 2-fold reduction in
718 volume compared to CAP-grown cells.
719 In addition to inducing a substantial change in size and volume, growth in pigeon guano
720 extract medium changes organ entry abilities of *C. neoformans* cells. We found that growing
721 cells in 10% guano medium, even without inducing small cell formation, resulted in more entry
722 into extra pulmonary organs than YNB-grown cells (**Fig. 7F**). Together, these data demonstrate
723 that *C. neoformans*'s environmental niche can make *C. neoformans* cells more prone to
724 dissemination and extrapulmonary organ entry and demonstrates the importance of considering
725 environmental niches when studying these opportunistic pathogens.
726
727

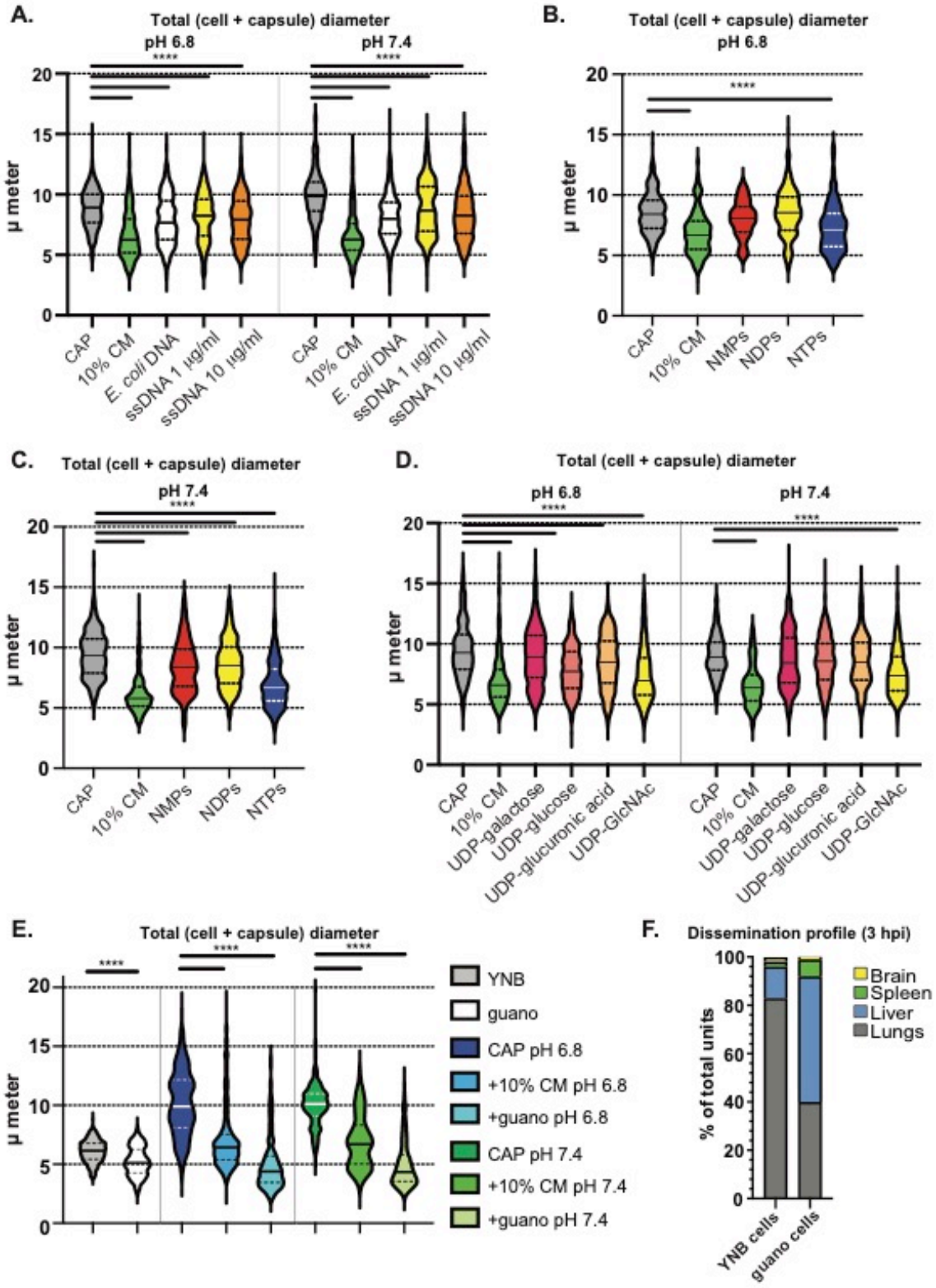

Figure 7: Diverse phosphate sources, including pigeon guano, induce small cell formation. (A) Total diameter (cell + capsule) measurements of cells after growth in CAP-

731 medium (10% Sabouraud's pH 6.8 (left) or 7.4 (right)) and supplementation with different DNA
732 sources. *E. coli* DNA concentration was 1 μg/ml and ssDNA at either 1 μg/ml (yellow) or 10
733 μg/ml (orange). **(B)** Total diameter measurements of CAP-grown cells after exposure to
734 nucleotide mono-, di-, or triphosphate pools at 200 μM total concentration (50 μM each of
735 adenine, cysteine, guanine, and uridine mono-, di-, or triphosphates) following growth at pH 6.8
736 or (**C)** pH 7.4. **(D)** Total diameter measurements of CAP-grown cells after exposure to UDP
737 sugars at pH 6.8 (left) or pH 7.4 (right). **(E)** Total diameter measurements of CAP-grown cells
738 after exposure to pigeon guano extract medium. **(F)** Organ distribution following tail vein
739 infection of *C. neoformans* cells grown in either YNB or pigeon guano extract medium. Panels
740 **A-E**: P-values calculated using Mann-Whitney test; N = 3 biological replicates per experiment
741 and >100 cells measured per replicate. The solid line represents the population median and the
742 dotted lines the 25th and 75th percentiles. The solid line represents the population median and
743 the dotted lines the 25th and 75th percentiles. All comparisons marked as significant represent
744 populations for which the 95% confidence interval does not overlap. ****$p<0.0001$.
745

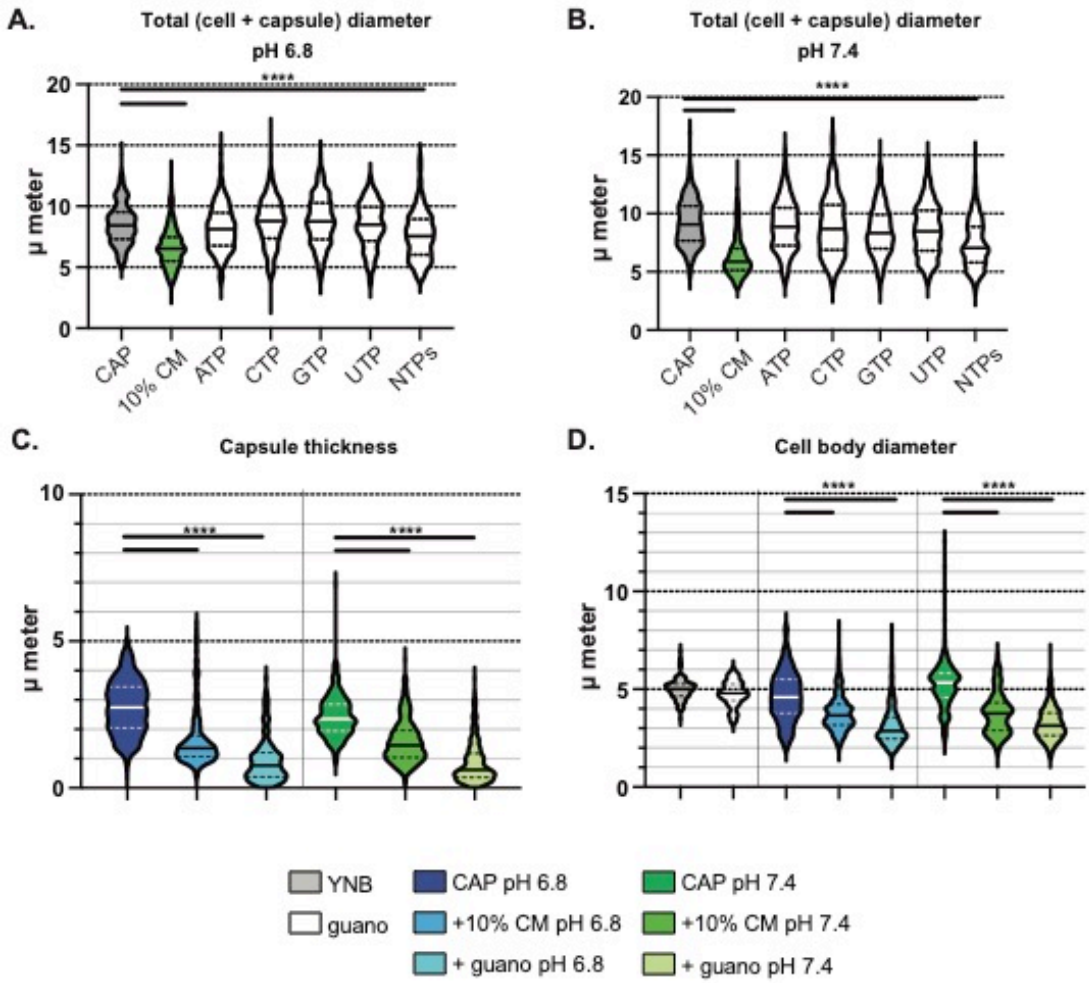

Supplemental Figure 6: Phosphate is sufficient to induce cell body diameter and capsule thickness reduction in alkaline capsule-inducing medium and is required for morphogenesis *in vivo*. Total diameter measurements of CAP-grown cells (pH 6.8 in **A**, pH 7.4 in **B**) after exposure to ATP, CTP, GTP, UTP at 200 μM or a pool of NTPs sy 200 μM total concentration (50 μM each of adenine, cysteine, guanine, and uridine triphosphates). **(C)** Capsule thickness (calculated using the formula (total diameter – cell body diameter)/2)) of CAP-grown cells (pH 6.8 on left, pH 7.4 on right) induced to form small cells in guano medium. **(D)** Cell body diameter of CAP-grown cells (pH 6.8 on left, pH 7.4 on right) induced to form small cells in guano medium. P-values calculated using Mann-Whitney test; N = 3 biological replicates per experiment and >100 cells measured per replicate. The solid line represents the population median and the dotted lines the 25th and 75th percentiles. The solid line represents the population median and the dotted lines the 25th and 75th percentiles. All comparisons

759 marked as significant represent populations for which the 95% confidence interval does not
760 overlap. ****$p<0.0001$.
761

762 **DISCUSSION:**

763 Here we demonstrate the formation of a new inducible morphotype that readily enters
764 and survives in extrapulmonary organs. Since these cells are transcriptionally distinct (**Fig. 5**)
765 and formed in response to extracellular signals (**Fig. 5, 6, 7**), we argue that they represent a
766 separate morphotype rather than part of a continuum of variously sized cells. Given their
767 importance for dissemination and extrapulmonary organ invasion and proliferation, we suggest
768 the name "seed cells" for this morphotype.

769 While seed cells are far from the only smaller-sized morphotype in *C. neoformans*, there
770 are notable distinct differences between seed cells and other morphotypes. Microcells, at
771 approximately 1 micron in diameter, are smaller than seed cells (Feldmesser et al., 2001). Drop
772 cells, while similar in shape, are described as metabolically inactive (Alanio et al., 2015a), which
773 seed cells are decidedly not. Cell division is required for small cell formation *in vitro*, since if we
774 do not add fresh growth medium when inducing small cells *in vitro*, the median population
775 diameter does not shift (**Fig. 6B**). One possibility is that seed cells and Titan daughter cells
776 ("titanides") (Zhou et al., 2020) are the same, independently described morphotype. We cannot
777 completely eliminate the possibility *in vivo*, but a key difference *in vitro* is that seed cell
778 formation does not require Titan cells. We can obtain small cells *in vitro* without inducing titan
779 cells beforehand (**Fig. 6**). In other ways, titanides are similar to seed cells, particularly their
780 hypothesized role in dissemination. Seed cells are also about the same size as "drop" cells
781 (Alanio et al., 2015b). These cells were isolated due to high non-cytoplasmic levels of the
782 glutathione stain CMFDA, which measures oxidative stress response. Drop cells are not thought
783 to be viable (Alanio et al., 2015b), while seed cells require nutrients for induction.

784 This work and others' underscore the critical importance of phenotypic heterogeneity in
785 the dissemination process. Heterogeneity in the form of antigen or phase switching is common
786 in bacteria (van der Woude and Bäumler, 2004) and parasite infections (Deitsch et al., 1999;
787 Ward et al., 1999). *C. neoformans* and other fungi exhibit incredible morphotype diversity but do
788 not, to our knowledge, exhibit classic antigenic switching. The closest comparable example
789 could be the adhesin *EPH* gene family regulation in *Candida glabrata* (López-Fuentes et al.,
790 2018), a diverse family of subtelomeric genes whose epigenetic regulation bears some
791 resemblance to the *var* gene family of *Plasmodium falciparum* (Kim, 2012). Instead, fungi shift
792 their surface antigens in response to environmental changes (Ballou et al., 2016; Hommel et al.,
793 2018; Trevijano-Contador et al., 2018) or through morphological changes (Fernandes et al.,
794 2018) such as spore (Botts et al., 2009), titan cell (Okagaki et al., 2010), drop cells (Alanio et al.,
795 2015a), micro cell (Feldmesser et al., 2001) and seed cell formation in *C. neoformans*.

796 Changes to mannose exposure on the *C. neoformans* cell surface seems to be one of
797 the more important changes for seed cells' interactions with the host immune system. Prior data
798 supporting the importance of mannose recognition and mannose-binding lectin by the host
799 during cryptococcosis is contradictory (Eisen et al., 2008; Fang et al., 2015). Despite the
800 increased mannose exposure on small *ex vivo* cells, we did not see significant MBL-binding to
801 cryptococcal cells. This may be because mannose-binding lectin is abundant in serum but we
802 analyzed fungal cells from perfused lung tissue. We found increased surfactant protein D (SPD)
803 binding of small and mid *ex vivo* cells compared with large *ex vivo* cells (**Fig. 3A**), and SPD can
804 bind to mannose-rich microbial features (Sahly et al., 2002). Mannose receptor-deficient mice
805 are more susceptible to *C. neoformans* infection (Dan et al., 2008). However, mannose
806 recognition via the mannose receptor was dispensable for murine, but not primary human,
807 macrophage phagocytosis of *C. neoformans and C. gattii* cells *in vitro* (Lim et al., 2018).
808 Mannose recognition depends on a given fungal cell's morphotype: the addition of exogenous
809 mannan reduced macrophage association with seed cells, but not large *ex vivo* cells or small
810 YNB-grown cells. Increased mannose exposure may result in a balance between host and
811 microbe: in places such as the liver, increased mannose-dependent uptake (**Fig. 3G**) is
812 countered by robust seed cell growth within the organ and the attempted fungal sequestration
813 backfiring on the host (**Fig. 3F**).
814 Our data also indicate that growth conditions dramatically influence dissemination ability
815 independent of size. Namely, cells originating from more stressful environments such as host
816 lungs or host-like *in vitro* conditions were better primed for survival and dissemination *in vivo*.
817 Capsule formation was not sufficient to facilitate organ entry (**Fig. 4A**) but did allow modest
818 increase in blood survival (**Fig. 4E**), while YNB-grown cells were deficient in both organ entry
819 and blood growth. These data suggest that efficient organ entry requires that cryptococcal cells
820 adopt smaller cell and capsule morphologies (**Fig. 4A**), stress resistance that will prime them for
821 survival in the blood and tissue (Alanio et al., 2015b; Ngamskulrungroj et al., 2012), and cell
822 surface changes.
823 Nutritional immunity is an important aspect of the host-pathogen arms race. This has
824 classically been associated with transition metals such as iron (Hood and Skaar, 2012).
825 However, phosphate availability is also tied to virulence (Kretschmer et al., 2014; Lev et al.,
826 2017). Here we find that phosphate is sufficient to induce seed cells at pHs where phosphate is
827 more likely to be limiting (**Fig. 6**).
828 Phosphate is essential for cell homeostasis and growth, and its acquisition is tightly
829 controlled in microbes that absorb fluctuating levels of phosphate from their surroundings

830 (Kohler et al., 2020; Lev and Djordjevic, 2018). Phosphate is critical for *Candida albicans*
831 morphogenesis (hyphal formation), stress resistance, and tissue invasion (Ikeh et al., 2016; Liu
832 et al., 2018). Phosphate acquisition is also essential for survival in the blood and dissemination
833 to the brain (Lev et al., 2017). *Cryptococcus* relies on a proton gradient to import phosphate
834 (Lev and Djordjevic, 2018) and therefore survives poorly in the alkaline (pH 7.4) bloodstream
835 where its ability to upregulate phosphate acquisition machinery is impaired (Lev et al., 2017).
836 Our results suggest that increased phosphate availability also impacts dissemination at an even
837 earlier stage by mediating the emergence of seed cells within the lungs (**Fig. 7**). We observed
838 an order of magnitude decrease in lung pH over the course of infection, which could also
839 enhance acquisition of phosphate and other nutrients (Lev et al., 2017) or independently
840 repress capsule growth (Farhi et al., 1970; O'Meara and Alspaugh, 2012) while still permitting
841 seed cell formation.
842 *PHO4* is not necessary for seed cell formation at pH 6.8. There could be at least two
843 pathways that control seed cell formation, with one phosphate-induced and one occurring at
844 acidic pH. Alternatively, the rewiring of the Pho4-controled genetic network at acidic pH
845 removes Pho4-dependence of seed cell formation-driving genetic factors. These formation
846 signals might or might not be present at both acidic and alkaline pH – pigeon guano and
847 conditioned medium both still induce seed cell formation at a range of pHs – but this will be a
848 fruitful area for future investigation.
849 Another source of variation within a population, which is sometimes linked to
850 morphology, is fungal cell ploidy. Ploidy serves as a driver of adaptation, in-host survival, and
851 pathogenicity in multiple fungal species (Gerstein et al., 2015; Okagaki and Nielsen, 2012;
852 Selmecki et al., 2015). Of our *ex vivo* populations, only large cells contain >2N cells (**Fig. S2**),
853 and even within the large cell population, the majority of cells are 2N, which could be either cells
854 in the G2 phase of mitosis or smaller titan cells. Intermediate cells display the DNA content
855 profile of actively growing haploid yeast cells (Todd et al., 2018). We therefore think that
856 comparisons between seed and intermediate *ex vivo* cells are likely independent of ploidy.
857 There are some notable limitations to our study. For example, we did not initially define
858 the subpopulations within the lungs based on clear biological criteria, but rather sorted cross-
859 sections of the population of fungal cells proliferating within the lungs. Small *ex vivo* “seed” cells
860 correspond with the size of disseminated cells in the brain, but intermediate and large cells are
861 based on arbitrary size cutoffs designed to distinguish them from small cells. Clearer definitions
862 of fungal subpopulations within the lungs and analysis of their dissemination would enhance our
863 understanding of systemic cryptococcosis. Furthermore, *C. neoformans* faces multiple

bottlenecks during dissemination, including escaping the lungs. *C. neoformans* can escape the lung mucosa to access the bloodstream by crossing lung epithelial cells or via the Trojan horse mechanism within macrophages (Denham and Brown, 2018). We focused on extrapulmonary organ entry rather than examining lung escape by seed cells directly. However, seed cells are more likely to be phagocytosed, which may lead to increased Trojan horse dissemination. We also find that in late infection (17 dpi), the total diameter of cells in the blood shows a size distribution similar to the lungs (**Fig. 1E**), suggesting that pulmonary escape may be less of a bottleneck than previously thought.

Phenotypic heterogeneity is an important microbial property that facilitates severe, disseminated infections (Zaragoza, 2011; Zhou and Ballou, 2018). Here we demonstrate that an individual morphotype, the seed cell, is prone to disseminate and shows an increased ability to enter extrapulmonary organs. Seed cells' dissemination ability is consistent with observations in humans (Fernandes et al., 2018), in that phenotypic heterogeneity strongly influences clinical outcome. Small *C. neoformans* cells are also found in the brains of human patients with cryptococcal meningitis (Xie et al., 2012). Overall, seed cells represent a new inducible morphotype formed in response to phosphate and other signals. Infection-induced phosphate availability could establish a feed-forward loop that results in self-propagation of *C. neoformans* dissemination. Moreover, conditions in *C. neoformans*'s environmental niche can induce seed cell formation and increase organ entry, thus increasing disease-causing potential for even an "accidental" pathogen.

ACKNOWLEDGEMENTS:

This work was supported by research grant R01AI130248 from the National Institutes of Health to J.C.S.B. S.T.D. was supported by grant T32AI055434 from the National Institutes of Health. Flow cytometry work was supported by the University of Utah Flow Cytometry Facility through the National Cancer Institute Award Number 5P30CA042014-24 and by the National Center for Research Resources of the National Institutes of Health under Award Number 1S10RR026802-01. RNA sequencing and analysis was performed by the High-Throughput Genomics and Bioinformatics Analysis Facility, a part of the Huntsman Cancer Institute at the University of Utah. Generation of the *pho4*Δ #1 clone was constructed in the Madhani laboratory with support from National Institutes of Health funding (R01AI100272). We would also like to thank Dr. Kyla Ost for her valuable input regarding the analysis of opsonin-binding via flow

cytometry. We would also like to thank Dr. Matthew Rondina and Dr. Alicia Eustes for their assistance with *in vivo* platelet depletion.

AUTHOR CONTRIBUTIONS:

S.T.D. and J.C.S.B. conceived and designed the experiments. S.T.D., B.B., K.Y.C., M.A.W., J.M.B., and J.C.S.B. performed the experiments. S.T.D., B.B., and J.C.S.B. analyzed the data. S.T.D. and J.C.S.B. wrote the paper. S.T.D., B.B., K.Y.C., M.A.W., and J.C.S.B. edited the paper.

DECLARATION OF INTERESTS:

The authors have no competing interests to declare.

METHODS:

Fungal strains and growth media

The following strains were used in this study: KN99α (Brown lab stock which was also the background for mutant strains), Bt63 (Brown lab stock, NCBI:txid1295841), 52D (ATCC 24067), R265 (ATCC MYA4093), WM276 (ATCC MYA-4071).

The following growth media were used in this study: YNB medium (yeast nitrogen base without amino acids [Difco catalog no. 291940], 2% glucose), CAP medium (10% Sabouraud's dextrose [Difco catalog no. 238230], buffered with 50 mM HEPES (pH 7.4) or MES (pH 6.3)), Titan cell medium (5% Sabouraud's dextrose, 10% fetal calf serum (GenClone catalog no. 25-550), 15 μM sodium azide, 50 mM HEPES (pH 7.4)).

***In vitro* small cell induction assay**

To screen for factors that facilitated shifts in cell size, we picked single colonies from *C. neoformans* cells streaked on YPAD agar and cultured them overnight (12-18 hours) in YNB medium at 30 °C. We then sub-cultured those cells into YNB medium, CAP medium, or titan cell medium for 24 hours at an initial cell density of 10^5 cells/mL. YNB- and CAP-grown cells were cultured at 37 °C, while titan cell medium-grown cells were cultured at 37 °C and 5% CO_2. At this stage, conditioned medium (CM) was collected from the 24-hour YNB cultures by pelleting the fungal cells and filtering (0.22 μm pore size) the supernatant. 450 μl of the CAP and titan cell media cultures were sub-cultured into 450 μl fresh media and 50 μl (10% of the final

931 volume) of one of the following supplements solubilized in H_2O: 10% H_2O (vehicle control), CM,
932 1% CM, 50 µg GXM, 50 µM Qsp1 peptide (Peptide 2.0: NFGAPGGAYPW), 50 µM Qsp1
933 scrambled peptide (Peptide 2.0: AWAGYFPGPNG), 10% 1x PBS (phosphate-buffered saline),
934 10% YNB medium; the following YNB medium supplements were added to a final concentration
935 that equaled their concentrations in YNB medium: 2% glucose, 4.531 nM folic acid, 8.186 nM
936 biotin, 250.6 nM copper sulfate pentahydrate, 531.4 nM riboflavin, 602.4 nM potassium iodide,
937 839.5 nM calcium pantothenate, 971.3 nM Sodium molybdate dihydrate, 1.186 µM thiamine
938 hydrochloride, 1.233 µM ferric chloride hexahydrate, 1.458 µM p-aminobenzoic acid, 1.945 µM
939 pyridoxine hydrochloride, 2.477 µM zinc sulfate heptahydrate, 2.649 µM manganese sulfate
940 monohydrate, 3.249 µM niacin, 8.087 µM boric acid, 11.10 µM inositol, 901.1 µM calcium
941 chloride dihydrate, 1.711 mM sodium chloride, 4.154 mM magnesium sulfate heptahydrate,
942 7.348 mM potassium phosphate monobasic, and 37.8mM ammonium sulfate. The
943 supplemented cultures were incubated for another 24 hours at 37 °C, following which 400 µl
944 was aliquoted to estimate cell size by flow cytometry and another 400 µl was aliquoted to
945 measure cell and capsule size (see “fungal cell size measurements”) in India ink (Higgins
946 catalog no. 44201).
947
948 **Pigeon guano medium**
949 Pigeon guano was a gift from Michael Shapiro’s lab (University of Utah Department of Biology).
950 Following collection, it was lyophilized, then stored at room temperature until use. Lyophilized
951 guano was ground in a coffee grinder until a powder. Guano medium consisted of a 20% w/v
952 solution in water, which was boiled for 10 minutes, then filtered through first Whatman 3 mm
953 filter paper, then a 0.5 µm polystyrene filter, and finally a 0.2 µm polystyrene filter. Resultant
954 medium was stored at room temperature for up to four weeks.
955
956 **Phosphate source small cell induction assay**
957 We grew fresh colonies of KN99 cells overnight in YNB at 37°C, then subcultured at 10^5 cells/ml
958 in CAP-medium 10% Sabouraud’s buffered to either pH 7.4 with 50 mM HEPES or pH 6.8 with
959 50 mM Tris HCl). Cultures were grown 24 hours at 37°C, then diluted 1:1 with either 20% (w/v)
960 pigeon guano medium or fresh 10% Sabouraud’s of the appropriate pH containing the
961 phosphate source of interest (DNA; nucleotide mono-, di-, or triphosphates; or UDP sugars).
962
963 **Mouse infection models and fungal burden analysis**

964 For intranasal inoculations, ~8-week-old female C57BL/6NJ mice (Jackson Laboratory)
965 mice were anesthetized with ketamine/dexmedetomidine hydrochloride (Dexdomitor) delivered
966 intraperitoneally. They were then suspended by their front incisors on a horizontal strand of
967 thread. Unless otherwise indicated, mice were inoculated intranasally with $2.5x10^4$
968 *Cryptococcus* cells in 50 µl of 1XPBS using a micropipette. The inoculum was placed dropwise
969 onto a nasal flare before being inhaled by mice. Ten minutes later, mice were intraperitoneally
970 administered the reversal agent atipamezole (Antisedan).
971 For intravenous inoculations, ~8-week-old female C57BL/6NJ mice (Jackson
972 Laboratory) were warmed under a heat lamp before being placed in a restraint. Mice were
973 inoculated via the tail vein with 10^5 *C. neoformans* cells or beads in 200 µl of 1XPBS using 28-
974 gauge x 12.7 mm syringes. In order to competitively inhibit host interactions with fungal
975 components *in vivo*, we administered 400 µg of GXM (see "GXM isolation), mannan (Sigma-
976 Aldrich catalog no. M7504), β-glucan (Millipore Sigma catalog no. 1048288), the chitin monomer
977 N-acetyl glucosamine (Vector Laboratories S-9002), or polyinosinic acid (Poly(I)) (Sigma-Aldrich
978 catalog no. 26936-41-4) in 200 µl of 1XPBS 2-3 minutes prior to inoculation with fungal cells.
979 For intracranial inoculations, ~6-week-old female C57BL/6NJ mice (Jackson
980 Laboratories) were anesthetized with ketamine/dexmedetomidine hydrochloride as described
981 above. They were inoculated intracranially with 10^3 *C. neoformans* cells in 30 µl of 1XPBS via a
982 26-gauge 1/2-inch needle. Following inoculation, mice were intraperitoneally administered the
983 reversal agent atipamezole (Antisedan; ~0.0125 mg/g).
984 Nonperfused mice were euthanized by CO2 asphyxiation and cervical dislocation. Mice
985 that were intracardially perfused at time of death were anesthetized with isoflurane and perfused
986 in a nonrecirculating fashion before cervical dislocation. Fungal burden was assessed by
987 excising organs and homogenizing them in 5 mL 1XPBS, washing the probe in between
988 samples: 30 seconds 10% bleach, 45 seconds 70% EtOH, and 10 seconds sterile H_2O. Ten-fold
989 serial dilutions of organ homogenate were plated on Sabouraud's agar containing 10 mg/ml
990 gentamicin and 100 mg/ml carbenicillin and stored at 30°C for 3 days before counting CFUs.
991 All animal procedures were approved by the University of Utah Institutional Animal Care
992 and Use Committee.
993
994 **Fungal cell size measurements**
995 *C. neoformans* cells harvested from laboratory growth medium or infected mouse lungs
996 were fixed in 2% paraformaldehyde for 20 minutes. To visualize capsule, 4 µl of India ink with 4
997 µl of cell suspension on a microscope slide. At least 10 successive images were taken starting

998 at one edge of the coverslip and moving across to the opposite side, as smaller cells tended to
999 drift to the edge of the coverslips. Total diameter was measured from one edge of the capsule to
1000 the other. Cell body diameter was measured from one edge of the cell wall to the other. Capsule
1001 thickness was calculated as follows: capsule thickness = (total diameter – cell body diameter) /
1002 2. The total number of cells counted for a given experiment is indicated in the figure legends.
1003
1004 **FACS isolation of fungal cells**
1005 Mice were intranasally inoculated with *C. neoformans* KN99-mCherry (see "Mouse
1006 infection models"). At 14 dpi, lungs from 3 mice were excised and placed in 15 mL of 1XPBS.
1007 The three lungs were homogenized together using a mechanical tissue homogenizer. The
1008 homogenate was filtered first through a 70 μM cell strainer and then through a 40 μM cell
1009 strainer to prevent downstream clogging of the flow cytometer. Cells were centrifuged at 2195xg
1010 for 10 min. The supernatant was discarded and the pellet was resuspended in ~1mL 1XPBS.
1011 The suspension was filtered once more through a 70 μM cell strainer and was resuspended at
1012 ~$1x10^7$ cells/mL in 1XPBS for FACS (BD FACS Aria). The FACS gating scheme is represented
1013 in **Figure 2**.
1014
1015 **Isolation of polystyrene beads from mouse organs**
1016 Mice were intravenously administered (see "Mouse infection models") 10^5 green
1017 fluorescent polystyrene beads (Polysciences, Inc. catalog no. 17156-2 and 18241-2), and 3
1018 hours later the indicated organs were harvested. Organs were homogenized with a mechanical
1019 tissue homogenizer in 5 mL tissue lysis buffer (100 mM Tris-Cl pH 8.0, 200mM NaCl, 5mM
1020 EDTA, 0.2% (w/v) SDS), washing the probe in between samples: 15 seconds H_2O, 15 seconds
1021 70% EtOH, and 15 seconds fresh H_2O.
1022 Beads from each organ were concentrated via differential centrifugation. The
1023 homogenates were poured into a fresh 50 mL conical. The homogenization tubes were washed
1024 with 30 mL of H_2O and combined with the respective homogenized sample. The samples were
1025 filtered through cell strainers (70 μM pore size), after which another 10 mL of H_2O was passed
1026 through each strainer. The samples were centrifuged at 4480xg for 40 minutes. The supernatant
1027 was aspirated to the 5 mL mark and the samples were transferred to fresh 15 mL tubes
1028 containing 2 mL of 100% Percoll (GE Healthcare catalog no. 17-0891-01). Water was added to
1029 the 10 mL mark. The tubes were vortexed to mix and allowed to settle for 5 minutes before
1030 centrifugation at 1120xg for 45 minutes. The supernatant was aspirated to the 2 mL mark. 10
1031 mL of H2O was added to the samples before centrifuging at 4480xg for 20 minutes. The

1032 supernatant was aspirated and resuspended in 200-1000 µl 1XPBS for flow cytometry. Entire
1033 samples were analyzed to determine the number of beads per organ.
1034
1035 **Fungal cell staining and flow cytometry analysis**
1036 Between 10^5 and 10^6 *C. neoformans* cells harvested from laboratory growth medium or
1037 infected mouse lungs were pelleted and fixed in 2% paraformaldehyde for 20 minutes. Fixed
1038 cells were pelleted and washed twice with 1XPBS. Cells were then resuspended in 1XPBS and
1039 stained with the desired antibodies/lectins/fluorescent dye.
1040 To estimate DNA content, cells were stained for 10 minutes (room temperature) in 0.3
1041 µg/mL 1XPBS+0.1% triton X-100. Mid-log phase fungal cells grown in YNB medium +/- 80
1042 µg/mL benomyl (Agilent catalog no. PST-1245) for 24 hours were used to set 1C and 2C gates.
1043 Untreated mid-log phage fungal cells display two DAPI peaks (1C ad 2C), while benomyl
1044 prevents cell division and traps cells at 2C.
1045 To estimate fungal microbial associated molecular pattern exposure, cells were stained
1046 at room temperature with 5 µg/mL fluorescein-conjugated wheat-germ agglutinin (WGA, Vector
1047 Laboratories catalog no. FL-1021) for 15 minutes to detect exposed chitin or 50 µg/mL
1048 fluorescein-conjugated concanavalin A (ConA, Vector Laboratories catalog no. FL-1001) for 5
1049 minutes to detect exposed mannose.
1050 To estimate the percentage of cells bound by soluble host factors, we used the following
1051 antibodies: α-complement C3 (primary: mAb 11H9, ThermoFisher catalog no. MA1-40046;
1052 secondary: Mouse anti-Rat IgG2a, FITC, Thermofisher catalog no. 11-4817-82), α-surfactant
1053 protein D (primary: polyclonal, Abcam catalog no. ab203309; secondary: Donkey anti-Rabbit
1054 IgG, AlexaFluor 405, Abcam catalog no. ab175651), α-mannose binding lectin A (primary: mAb
1055 8G6, Hycult catalog no. HM1035; secondary: Mouse anti-Rat IgG2a, FITC, Thermofisher
1056 catalog no. 11-4817-82), α-mannose binding lectin C (primary: mAb 14D12, Abcam catalog no.
1057 ab106046; secondary: Mouse anti-Rat IgG2a, FITC, Thermofisher catalog no. 11-4817-82), α-
1058 IgM (mAb II/41, FITC, BD Biosciences catalog no. 553437), α-IgA (mAb 11-44-2, FITC,
1059 SouthernBiotech catalog no. 1165-02). Cells were stained with primary antibodies (1:50 dilution)
1060 for 30 minutes on ice. When a secondary antibody was required, primary antibody labeled cells
1061 were pelleted, washed twice with 1XPBS and stained with the secondary antibody (1:50 dilution)
1062 for 20 minutes on ice.
1063 After staining, cells were pelleted and washed twice with 1mL 1XPBS before being
1064 resuspended in 200-400 µl of 1XPBS for flow cytometry.
1065

1066 **GXM isolation**

1067 GXM was isolated as described previously (Wozniak and Levitz, 2009) with slight
1068 modifications. *C. neoformans* (KN99) cells were grown in 100 mL for 3 days at 37°C in YNB
1069 medium (YNB+2% glucose). Cells were centrifuged for 15 minutes at 12,000xg. The
1070 supernatant was filtered (0.45 µM pore size) and 50 mL of supernatant was transferred to a 250
1071 mL bottle. ~150 mL of 95% EtOH was added to the samples in 4-5 aliquots, mixing after each
1072 addition. Samples were stored at 4°C overnight to precipitate GXM. Samples were centrifuged
1073 for 30 minutes at 15,000xg, 4°C. The pellets were resuspended in 0.2M NaCl to a concentration
1074 of about 10 mg/mL (~50 mL per 250 mL bottle). Samples were transferred to a clean beaker
1075 stirred until samples were completely resuspended. 3 mg hexadecyltrimethylammonium
1076 bromide (CTAB) per 1mg precipitate was slowly added with stirring and low heat. Once
1077 solubilized, the samples were removed from heat and 250 mL of 0.05% CTAB was slowly
1078 added with stirring. The samples were moved to fresh 250 mL bottles and centrifuged at for 2
1079 hours at 11,000xg, 4°C. The supernatant was discarded and the pellet was washed in 150 mL
1080 of 10% EtOH. The samples were centrifuge for 20 minutes at 15,000xg, room temperature. The
1081 supernatant was discarded and the pellets were resuspended in 50 mL of 1M NaCl. The
1082 samples were transferred to a clean beaker and stirred until completely resuspended.
1083 Approximately 2 volumes of 95% EtOH was added dropwise with stirring to precipitate the GXM
1084 while leaving the CTAB in solution. The samples were centrifuged in fresh 250 mL bottles for 20
1085 minutes at 11,000xg, room temperature. The supernatant was discarded and the precipitate
1086 was dissolved in 2M NaCl. The resulting solution was placed in a snake-skin dialysis cassette
1087 with a 3,500 molecular weight cutoff (Thermo Fisher Scientific catalog no. 68035) and dialyzed
1088 overnight against 1M NaCl. The samples were subsequently dialyzed against distilled H_2O for
1089 14 days at 4°C. The distilled H_2O was changed every 1-2 hours for the first 2 days, and then 4-5
1090 times a day for the next 6 days. For the last 2-6 days, the water was changed 2-3 times a day.
1091 The dialyzed samples were lyophilized and stored at -80 °C.

1092

1093 **Cell-type specific depletion in mice**

1094 Hepatic and splenic macrophages were depleted from mice using clodronate liposomes.
1095 Mice were intravenously administered 200 µl of clodronate liposomes (Liposoma BV catalog no.
1096 C-010) or PBS control liposomes (Liposoma BV catalog no. P-010) 48 hours prior to inoculation
1097 with *C. neoformans* cells. Macrophage depletion efficiency in the liver and spleen was assessed
1098 on the day of inoculation via flow cytometry. Macrophages were identified as CD45+ (anti-

1099 CD45-efluor450, eBiosciences catalog no. 48-0451-82) and F4/80+ (anti-F4/80-APC,
1100 eBiosciences catalog no. 17-4801-80).
1101 Neutrophils were depleted from mice using anti-Ly6G antibodies. Mice were
1102 intraperitoneally administered 200 ug of anti-Ly6G (clone 1A8 BioXcell catalog no. BP0075-1)
1103 antibodies or PBS control at 24 and 2 hours prior to inoculation with *C. neoformans* cells.
1104 Neutrophil depletion efficiency in the blood was assessed on the day of inoculation via flow
1105 cytometry. Neutrophils were identified as CD45+ (anti-CD45-efluor450, eBiosciences catalog
1106 no. 48-0451-82), CD11b+ (anti-CD11b-APC, eBiosciences catalog no. 17-0112-82), and Ly6G+
1107 (anti-Ly6G-FITC, eBiosciences catalog no. 11-5931-82).
1108 Platelets were depleted from mice using anti-GPIbα antibodies. Mice were intravenously
1109 administered 80 µl of anti-GPIbα antibodies (Emfret catalog no. R300) or PBS control 24 hours
1110 prior to inoculation with *C. neoformans* cells. Platelet depletion efficiency was determined by
1111 Hemavet 950FS (Drew Scientific Group) analysis of blood collected by cheek bleed 10 minutes
1112 prior to anti-GPIbα administration and on the day of inoculation.
1113
1114 **Liver macrophage isolation and infection**
1115 Liver macrophages were isolated from 8- to 10-week-old female C57BL/6NJ mice
1116 (Jackson Laboratory) according to established procedures (Li et al., 2014). Isolated liver
1117 macrophages were resuspended in complete DMEM (Dulbecco's Modified Eagle's Medium,
1118 GenClone catalog no. 25-500) supplemented with 10% fetal bovine serum (FBS, (GenClone
1119 catalog no. 25-550) and 100 U/mL Penicillin/Streptomycin and seeded into a T-25 flask at a
1120 density of 8-10 × 10^6 cells/flask. Macrophages were allowed to settle and adhere for 4 hours in a
1121 mammalian tissue culture incubator (37 °C, 5% CO_2). Non-adherent cells were then removed
1122 from the dish by gently washing 3 times with 1XPBS (without divalent cations), leaving adherent
1123 macrophages. The media was replaced with 5 mL complete DMEM, and the cells were rested
1124 for 4 days. The media was replaced on the day after initial seeding, and then as needed.
1125 Fungal infection and association with liver macrophages was assessed using the
1126 following procedures. The media was aspirated from rested liver macrophages and the cells
1127 were washed once with 1XPBS. Macrophages were lifted from the plate by treating them with
1128 1mL Accutase (Corning catalog no. 25-058-CI) for ~5 minutes, tapping the plate to dislodge
1129 cells. 1 mL complete DMEM was added to the Accutase-treated cells, which were then
1130 centrifuged at 300xg for 5 minutes. Liver macrophages were resuspended cells in 0.5-1 mL
1131 complete DMEM and live cells were counted by mixing trypan blue (HyClone catalog no.
1132 SV30084.01) with cell suspension at a 1:1 ratio and counting clear cells on a hemocytometer.

1133 40,000 live cells/well were seeded into 96-well plates in complete DMEM. The liver
1134 macrophages were allowed to settle and adhere overnight.
1135 The next day, the inoculum was prepared by resuspending *C. neoformans* cells in 500 µl
1136 of 0.01% Direct Yellow 96 (AK Scientific 61725-08-4), vortexing briefly to mix, and incubating for
1137 5 minutes on the benchtop. *C. neoformans* cells stained with Direct Yellow 96 were pelleted,
1138 washed once with 1 mL 1XPBS, and resuspended at a concentration of $8x10^6$ cells/mL in
1139 serum-free DMEM. The supernatant was aspirated from the macrophages seeded in the 96-well
1140 plates and was replaced with 200 µl of serum-free DMEM. 10 µl of the inoculum ($8x10^4$ cells)
1141 was added to each well, resulting in a multiplicity of infection of 1:1. Macrophages and *C.*
1142 *neoformans* cells were co-cultured for 4 hours in a mammalian tissue culture incubator (37 °C,
1143 5% CO_2). The medium was then aspirated from each well, and the cells were washed three
1144 times with 100 µl of 1XPBS to remove non-macrophage associated fungal cells. The remaining
1145 cells were fixed in 100 µl of 4% paraformaldehyde for 10 min. The paraformaldehyde was then
1146 removed and the cells were washed twice with 100 µl of 1XPBS and stained with100 µl of DAPI
1147 (Sigma Aldrich catalog no. 28718-90-3) working solution (600 nM DAPI; 0.1% Triton X-100; in
1148 1XPBS) for 5 minutes. The DAPI working solution was then removed and cells were washed
1149 twice with 100 µl of 1XPBS. Finally, 100 µl of 1XPBS was added to the wells to prevent
1150 desiccation. Cells were imaged on a Nikon widefield microscope, and the number of
1151 macrophages with associated *C. neoformans* cell(s) were counted (green-fluorescent due to
1152 Direct Yellow 96). Six images were taken per well in the same relative positions and every
1153 imaged macrophage was scored as having a physically associated fungal cell(s) or not,
1154 resulting in 2263-3197 macrophages counted per experimental condition across three
1155 independent replicates.
1156 In order to asses liver macrophage killing of *C. neoformans* cells, liver macrophages
1157 were seeded in 96-well plates and infected with *C. neoformans* cells as described above. The
1158 plates containing *C. neoformans* and macrophages were incubated for 24 or 48 hours. After the
1159 desired time, the supernatant was collected from each well and transferred to a microcentrifuge
1160 tube. 200 µl of sterile distilled water was then added to each well in order to lyse the
1161 macrophages for 40 minutes at 37°C. The contents of each well were then mixed to collect
1162 every *C. neoformans* cell and combined with the respective supernatant now in a
1163 microcentrifuge tube. The wells were rinsed with 200 µl sterile PBS and added to the respective
1164 microcentrifuge tube. Serial dilutions of each of the well contents were plated on YPAD agar
1165 and incubated at 30°C for 2-3 days before counting CFUs. CFUs quantified at each timepoint
1166 were normalized to the CFUs in the inoculum in order to calculate the “% of input”. Each

1167 macrophage killing experiment was repeated on three different days with each experimental
1168 condition being performed in duplicate wells.
1169
1170 **Fungal survival in blood**
1171 We collected whole blood from 8- to 10-week-old female C57BL/6NJ mice
1172 (Jackson Laboratory) to assess *C. neoformans* survival in blood. Mice were anesthetized with
1173 isoflurane, and whole blood was collected by cardiac puncture using 28-gauge x 12.7 mm
1174 syringes pre-coated with 0.5M EDTA. Blood was immediately transferred to tubes containing
1175 heparin to achieve a final concentration of 30 units of heparin per mL of blood. 100 µl of blood
1176 was added to individual wells of a 96-well plate. 100 *C. neoformans* cells in 5 ul of 1XPBS were
1177 used to inoculate each well. The plates were incubated in a mammalian tissue culture incubator
1178 (37 °C, 5% CO_2) without shaking. At the indicated timepoint, the well contents were transferred
1179 to fresh microcentrifuge tubes. The wells were washed with 100 ul of 0.05M EDTA, which was
1180 then added to the respective microcentrifuge tube. The entire contents of the microcentrifuge
1181 tubes were plated on YPAD agar and incubated at 30°C for 2-3 days before counting CFUs.
1182 CFUs quantified at each timepoint were normalized to the CFUs in the inoculum in order to
1183 calculate the "% of input". Each experiment was repeated on three different days with each
1184 experimental condition being performed in duplicate wells.
1185
1186 **RNA isolation, sequencing, and analysis**
1187 RNA sequencing data is publicly available at NCBI GEO (Accession number:
1188 GSE152784). *C. neoformans* cells were harvested from laboratory media and from infected
1189 mouse lungs for RNA isolation and sequencing. Three replicates were sequenced for each
1190 sample with replicates being defined as follows. Approximately 10^7 cells were harvested from
1191 the indicated *in vitro* growth condition on three separate days. At least 10^6 *ex vivo* cells were
1192 isolated per sort gate each day (see "FACS isolation of fungal cells"). *Ex vivo* cells were isolated
1193 from the pooled lung homogenate of three mice. *Ex vivo* sample populations were isolated on
1194 two consecutive days and pooled for RNA isolation and sequencing, with the end result being
1195 that each sequenced *ex vivo* replicate represents fungal cells isolated from pools of six mice.
1196 RNA was isolated using phenol-chloroform extraction, followed by Qiagen RNeasy
1197 column-based cleanup. Fungal cells were pelleted, flash frozen in liquid nitrogen, and
1198 lyophilized until completely dry. Lyophilized cells were resuspended in 750 µl of TRIzol
1199 (ThermoFisher Scientific catalog no. 15596026) inside screw-cap microcentrifuge tubes.
1200 Approximately 50 µl of 1-mm and 150 µl of 0.5mm zirconium beads (BioSpec Products catalog

1201 no. 11079110z and 11079105z) were added to each sample and placed in a Biospec Products
1202 mini bead beater to lyse (12 x 2 min beating pulses, using sample blocks stored at -20 °C to
1203 prevent overheating). 150 µl of chloroform was added to the lysed samples and incubated for 2-
1204 3min at room temperature. Samples were centrifuged for 15 minutes at 12,000 x *g*, 4°C. The
1205 aqueous phase was transferred to a fresh tube and combined with 5-10 µg RNase-free
1206 glycogen as a carrier. 0.375 mL of isopropanol was added to each sample before incubating at
1207 least ~20 minutes on ice. The samples were centrifuged for 15 minutes at 12,000 x *g*, 4°C. The
1208 supernatant was discarded, and the isopropanol was removed by pipetting. The samples were
1209 then briefly air-dried before resuspension in 350 µl of RLT buffer (Qiagen RNeasy) and 350 µl
1210 70% EtOH. At this junction, samples were run through Qiagen's RNAeasy kit (Qiagen catalog
1211 no. 74104) with on-column DNase treatment.
1212 cDNA libraries were generated with the NEBNext Ultra II Directional RNA Library Prep
1213 with rRNA Depletion Kit (New England BioLabs catalog no. E7760) by the High Throughput
1214 Genomics Core at the University of Utah. Sample libraries were sequenced on the Illumina
1215 NovaSeq 6000. One set of samples (primarily the *ex vivo* small, medium, and large cells) were
1216 stored by the High Throughput Genomics Core at -80°C for six months prior to library
1217 construction and showed more degradation products than replicates stored at -80°C for one
1218 month. We therefore limited our analysis and interpretation of the data from these samples.
1219 The *Cryptococcus neoformans* var. grubii H99 genome and gene feature files were
1220 downloaded from Ensembl Fungi release 46 and the reference database was created using
1221 STAR version 2.7.2c with splice junctions optimized for 150 base pair reads (Dobin et al., 2013).
1222 Optical duplicates were removed from the paired end FASTQ files using clumpify v38.34 and
1223 reads were trimmed of adapters using cutadapt 1.16 (Martin, 2011). The trimmed reads were
1224 aligned to the reference database using STAR in two pass mode to output a BAM file sorted by
1225 coordinates. Mapped reads were assigned to annotated genes in the gene feature file using
1226 featureCounts version 1.6.3 (Liao et al., 2014). The output files from cutadapt, FastQC, Picard
1227 CollectRnaSeqMetrics, STAR and featureCounts were summarized using MultiQC to check for
1228 any sample outliers (Ewels et al., 2016). Differentially expressed genes were identified using a
1229 5% false discovery rate with DESeq2 version 1.24.0 (Love et al., 2014). Differentially expressed
1230 genes were run through FungiDB Gene Ontology (GO) Enrichment analysis, selecting for
1231 "biological process" with a p-value cutoff of 0.05 (Basenko et al., 2018; Stajich et al., 2012).
1232 Venn Diagrams were made with software from the Van de Peer group at Ghent University
1233 (http://bioinformatics.psb.ugent.be/webtools/Venn/).
1234

1235 **Lung pH measurements**

1236 To measure lung tissue pH, mouse lungs were excised and immediately pierced with a
1237 micro pH electrode (Orion (ThermoFisher Scientific) catalog no. 9863BN). The electrode was
1238 completely embedded in the lung tissue before taking pH readings. Two readings were taken
1239 per mouse. One reading was taken from the left lobe of the lungs and a second reading was
1240 taken from one of the right lobes. These two readings were averaged to estimate lung pH for a
1241 given mouse.

1242

1243 **Construction of the KN99:*pho4*Δ strains**

1244 The KN99:*pho4*Δ (*CNAG_06751*Δ) strains were constructed via homologous
1245 recombination-based replacement of the *pho4* genomic sequence with a nourseothicin
1246 resistance marker. The KN99:*pho4*Δ #1 strain was obtained from the KN99 gene deletion library
1247 (Fungal Genetics Stock Center, 2015 Madhani plates). The KN99:*pho4*Δ #2 strain was
1248 generated by PCR amplification of the nourseothicin resistance marker and ~1,000 base pair
1249 flanking regions from the KN99:*pho4*Δ #1 strain (primers used to amplify the knock-out
1250 construct: Forward: 5' AAAACGGCTGAAGGCTCGTTCT3', Reverse:
1251 CTTCTGCAAGGTGAAGTTCACG). The resulting pho4 knock-out cassette was used to
1252 transform wild-type KN99 cells via biolistic transformation as described previously (Davidson et
1253 al., 2000). Putative transformants were PCR-verified by confirming the absence of the *pho4*
1254 open reading frame (Primers to verify the absence of the open reading frame: Forward:
1255 5'CCATCTCAGATACCAACTCGCC', Reverse: 5'CAATTTGCTGAGAGCCATAGGC3') and the
1256 integration of the knock-out construct at the correct site (Primers to verify the correct 5'
1257 integration site: Forward: 5'AGAGCTATATGGTATGACGAAC3', Reverse:
1258 5'TGTGCTGATCATCCGATGCCAC3' and the correct 3' integration site: Forward
1259 5'TGTGGAGGATGGTGGGGAATAG3', Reverse: 5'GGACGTGAGCCAATAAGTTCCT3'.

1260

1261 **Statistics**

1262 All statistical analyses, with the exception of RNA sequencing analysis, were performed
1263 with GraphPad Prism 8 software. Hypothesis-driven experimental comparisons were analyzed
1264 by unpaired t-test or one-way ANOVA and uncorrected Fisher's LSD if the data held a Gaussian
1265 distribution and a Mann-Whitney U-test if the data were not Gaussian. For experiments with
1266 large sample sizes (e.g. cell size measurements), statistical significance is shown only if the
1267 95% confidence intervals of the median compared samples does not overlap. *In vitro*
1268 experiments were replicated three times unless otherwise stated. *In vivo* (murine infection)

1269 experiments were replicated twice unless otherwise stated. Sample sizes are stated in the figure
1270 legend.
1271

1272 **Phosphate extraction and measure**

1273 To determine the amount of phosphate within cells, we grew cells in CAP medium and
1274 performed a standard small cell induction assay. We harvested 3 x 10^7 total cells by
1275 centrifugation, washed briefly in water to remove any excess growth medium, then froze in liquid
1276 nitrogen. Samples were then lyophilized overnight, then resuspended in 300 μl MilliQ water,
1277 vortexed for 30 seconds on/30 seconds off (on ice) for 30 minutes, then tested for phosphate
1278 concentration using the Phosphate Colorimetric Kit (Sigma-Aldrich, catalog no. MAK030-1KT)
1279 according to the manufacturer's instructions.
1280

1281 **REFERENCES:**

1282 Agustinho, D.P., Miller, L.C., Li, L.X., and Doering, T.L. (2018). Peeling the onion: the outer
1283 layers of Cryptococcus neoformans. Mem Inst Oswaldo Cruz *113*, e180040.
1284 Aimanianda, V., Bayry, J., Bozza, S., Kniemeyer, O., Perruccio, K., Elluru, S.R., Clavaud, C.,
1285 Paris, S., Brakhage, A.A., Kaveri, S.V., *et al.* (2009). Surface hydrophobin prevents
1286 immune recognition of airborne fungal spores. Nature *460*, 1117-1121.
1287 Alanio, A., Vernel-Pauillac, F., Sturny-Leclère, A., and Dromer, F. (2015a). Cryptococcus
1288 neoformans host adaptation: toward biological evidence of dormancy. mBio *6*.
1289 Alanio, A., Vernel-Pauillac, F., Sturny-Leclère, A., and Dromer, F. (2015b). *Cryptococcus*
1290 *neoformans* Host Adaptation: Toward Biological Evidence of Dormancy. mBio *6*,
1291 e02580-02514.
1292 Albuquerque, P., Nicola, A.M., Nieves, E., Paes, H.C., Williamson, P.R., Silva-Pereira, I., and
1293 Casadevall, A. (2013). Quorum sensing-mediated, cell density-dependent regulation of
1294 growth and virulence in *Cryptococcus neoformans*. mBio *5*, e00986-00913.
1295 Altamirano, S., Jackson, K.M., and Nielsen, K. (2020). The interplay of phenotype and genotype
1296 in Cryptococcus neoformans disease. Biosci Rep *40*, BSR20190337.
1297 André, A.C., Laborde, M., and Marteyn, B.S. (2022). The battle for oxygen during bacterial and
1298 fungal infections. Trends Microbiol.
1299 Ballou, E.R., Avelar, G.M., Childers, D.S., Mackie, J., Bain, J.M., Wagener, J., Kastora, S.L.,
1300 Panea, M.D., Hardison, S.E., Walker, L.A., *et al.* (2016). Lactate signalling regulates
1301 fungal β-glucan masking and immune evasion. Nat Microbiol *2*, 16238.
1302 Basenko, E.Y., Pulman, J.A., Shanmugasundram, A., Harb, O.S., Crouch, K., Starns, D.,
1303 Warrenfeltz, S., Aurrecoechea, C., Stoeckert, C.J., Jr., Kissinger, J.C., *et al.* (2018).
1304 FungiDB: An Integrated Bioinformatic Resource for Fungi and Oomycetes. J Fungi
1305 (Basel) *4*, 39.
1306 Becquer, A., Trap, J., Irshad, U., Ali, M.A., and Claude, P. (2014). From soil to plant, the
1307 journey of P through trophic relationships and ectomycorrhizal association. Front Plant
1308 Sci *5*, 548.

1309 Beis, I., and Newsholme, E.A. (1975). The contents of adenine nucleotides, phosphagens and
1310 some glycolytic intermediates in resting muscles from vertebrates and invertebrates.
1311 Biochem J *152*, 23-32.
1312 Bojarczuk, A., Miller, K.A., Hotham, R., Lewis, A., Ogryzko, N.V., Kamuyango, A.A., Frost,
1313 H., Gibson, R.H., Stillman, E., May, R.C*., et al.* (2016). *Cryptococcus neoformans*
1314 intracellular proliferation and capsule size determines early macrophage control of
1315 infection. Sci Rep *6*, 21489.
1316 Botts, M.R., Giles, S.S., Gates, M.A., Kozel, T.R., and Hull, C.M. (2009). Isolation and
1317 Characterization of *Cryptococcus neoformans* Spores Reveal a Critical Role for Capsule
1318 Biosynthesis Genes in Spore Biogenesis. Eukaryot Cell *8*, 595-605.
1319 Botts, M.R., and Hull, C.M. (2010). Dueling in the lung: how Cryptococcus spores race the host
1320 for survival. Curr Opin Microbiol *13*, 437-442.
1321 Brinkmann, V., Reichard, U., Goosmann, C., Fauler, B., Uhlemann, Y., Weiss, D.S., Weinrauch,
1322 Y., and Zychlinsky, A. (2004). Neutrophil extracellular traps kill bacteria. Science *303*,
1323 1532-1535.
1324 Broadley, S.P., Plaumann, A., Coletti, R., Lehmann, C., Wanisch, A., Seidlmeier, A., Esser, K.,
1325 Luo, S., Ramer, P.C., Massberg, S*., et al.* (2016). Dual-Track Clearance of Circulating
1326 Bacteria Balances Rapid Restoration of Blood Sterility with Induction of Adaptive
1327 Immunity. Cell Host Microbe *20*, 36-48.
1328 Brown, G.D., Herre, J., Williams, D.L., Willment, J.A., Marshall, A.S., and Gordon, S. (2003).
1329 Dectin-1 mediates the biological effects of beta-glucans. J Exp Med *197*, 1119-1124.
1330 Bulmer, G.S., and Sans, M.D. (1967). Cryptococcus neoformans. II. Phagocytosis by human
1331 leukocytes. J Bacteriol *94*, 1480-1483.
1332 Casadevall, A., Coelho, C., Cordero, R.J.B., Dragotakes, Q., Jung, E., Vij, R., and Wear, M.P.
1333 (2019). The capsule of *Cryptococcus neoformans*. Virulence *10*, 822-831.
1334 Chaconas, G., Castellanos, M., and Verhey, T.B. (2020). Changing of the guard: How the Lyme
1335 disease spirochete subverts the host immune response. The Journal of biological
1336 chemistry *295*, 301-313.
1337 Chang, Y.C., Stins, M.F., McCaffery, M.J., Miller, G.F., Pare, D.R., Dam, T., Paul-Satyaseela,
1338 M., Kim, K.S., and Kwon-Chung, K.J. (2004). Cryptococcal yeast cells invade the central
1339 nervous system via transcellular penetration of the blood-brain barrier. Infect Immun *72*,
1340 4985-4995.
1341 Charlier, C., Chrétien, F., Baudrimont, M., Mordelet, E., Lortholary, O., and Dromer, F. (2005).
1342 Capsule structure changes associated with *Cryptococcus neoformans* crossing of the
1343 blood-brain barrier. Am J Pathol *166*, 421-432.
1344 Charlier, C., Nielsen, K., Daou, S., Brigitte, M., Chretien, F., and Dromer, F. (2009). Evidence of
1345 a role for monocytes in dissemination and brain invasion by Cryptococcus neoformans.
1346 Infect Immun *77*, 120-127.
1347 Chen, S.H.M., Stins, M.F., Huang, S.H., Chen, Y.H., Kwon-Chung, K.J., Chang, Y., Kim, K.S.,
1348 Suzuki, K., and Jong, A.Y. (2003). Cryptococcus neoformans induces alterations in the
1349 cytoskeleton of human brain microvascular endothelial cells. J Med Microbiol *52*, 961-
1350 970.
1351 Chen, Y., Li, C., Sun, D., Strickland, A.B., Liu, G., and Shi, M. (2021). Quantitative analysis
1352 reveals internalisation of Cryptococcus neoformans by brain endothelial cells in vivo.
1353 Cell Microbiol *23*, e13330.

1354 Chun, C.D., Brown, J.C.S., and Madhani, H.D. (2011). A Major Role for Capsule-Independent
1355 Phagocytosis-Inhibitory Mechanisms in Mammalian Infection by *Cryptococcus*
1356 *neoformans*. Cell Host Microbe *9*, 243-251.
1357 Chung, K.Y., and Brown, J.C.S. (2020). Biology and function of exo-polysaccharides from
1358 human fungal pathogens. Curr Clin Microbiol Rep *7*, 1-11.
1359 Crabtree, J.N., Okagaki, L.H., Wiesner, D.L., Strain, A.K., Nielsen, J.N., and Nielsen, K. (2012).
1360 Titan cell production enhances the virulence of Cryptococcus neoformans. Infect Immun
1361 *80*, 3776-3785.
1362 Dambuza, I.M., Drake, T., Chapuis, A., Zhou, X., Correia, J., Taylor-Smith, L., LeGrave, N.,
1363 Rasmussen, T., Fisher, M.C., Bicanic, T.*, et al.* (2018). The Cryptococcus neoformans
1364 Titan cell is an inducible and regulated morphotype underlying pathogenesis. PLoS
1365 pathogens *14*, e1006978-e1006978.
1366 Dan, J.M., Kelly, R.M., Lee, C.K., and Levitz, S.M. (2008). Role of the mannose receptor in a
1367 murine model of *Cryptococcus neoformans* infection. Infect Immun *76*, 2362-2367.
1368 Davidson, R.C., Cruz, M.C., Sia, R.A., Allen, B., Alspaugh, J.A., and Heitman, J. (2000). Gene
1369 disruption by biolistic transformation in serotype D strains of Cryptococcus neoformans.
1370 Fungal Genet Biol *29*, 38-48.
1371 Davis, K.M. (2018). All Yersinia Are Not Created Equal: Phenotypic Adaptation to Distinct
1372 Niches Within Mammalian Tissues. Front Cell Infect Microbiol *8*, 261.
1373 Davis, K.M., Mohammadi, S., and Isberg, R.R. (2015). Community behavior and spatial
1374 regulation within a bacterial microcolony in deep tissue sites serves to protect against
1375 host attack. Cell Host Microbe *17*, 21-31.
1376 Deitsch, K.W., del Pinal, A., and Wellems, T.E. (1999). Intra-cluster recombination and var
1377 transcription switches in the antigenic variation of Plasmodium falciparum. Mol Biochem
1378 Parasitol *101*, 107-116.
1379 Denham, S.T., and Brown, J.C.S. (2018). Mechanisms of Pulmonary Escape and Dissemination
1380 by Cryptococcus neoformans. J Fungi (Basel) *4*, 25.
1381 Denham, S.T., Verma, S., Reynolds, R.C., Worne, C.L., Daugherty, J.M., Lane, T.E., and
1382 Brown, J.C.S. (2018). Regulated release of cryptococcal polysaccharide drives virulence
1383 and suppresses immune infiltration into the central nervous system. Infect Immun *86*.
1384 Diamond, R.D., and Bennett, J.E. (1973). Growth of Cryptococcus neoformans Within Human
1385 Macrophages In Vitro. Infect Immun *7*, 231-236.
1386 Dobin, A., Davis, C.A., Schlesinger, F., Drenkow, J., Zaleski, C., Jha, S., Batut, P., Chaisson,
1387 M., and Gingeras, T.R. (2013). STAR: ultrafast universal RNA-seq aligner.
1388 Bioinformatics *29*, 15-21.
1389 Dosch, M., Gerber, J., Jebbawi, F., and Beldi, G. (2018). Mechanisms of ATP Release by
1390 Inflammatory Cells. Int J Mol Sci *19*.
1391 Eisen, D.P., Dean, M.M., O'Sullivan, M.V., Heatley, S., and Minchinton, R.M. (2008). Mannose-
1392 binding lectin deficiency does not appear to predispose to cryptococcosis in non-
1393 immunocompromised patients. Med Mycol *46*, 371-375.
1394 Elliott, M.R., Chekeni, F.B., Trampont, P.C., Lazarowski, E.R., Kadl, A., Walk, S.F., Park, D.,
1395 Woodson, R.I., Ostankovich, M., Sharma, P.*, et al.* (2009). Nucleotides released by
1396 apoptotic cells act as a find-me signal to promote phagocytic clearance. Nature *461*, 282-
1397 286.
1398 Emmons, C.W. (1955). Saprophytic sources of Cryptococcus neoformans associated with the
1399 pigeon (Columba livia). Am J Hyg *62*, 227-232.

1400 Ewels, P., Magnusson, M., Lundin, S., and Kaller, M. (2016). MultiQC: summarize analysis
1401 results for multiple tools and samples in a single report. Bioinformatics *32*, 3047-3048.
1402 Fang, W., Fa, Z., and Liao, W. (2015). Epidemiology of *Cryptococcus* and cryptococcosis in
1403 China. Fungal Genet Biol *78*, 7-15.
1404 Farhi, F., Bulmer, G.S., and Tacker, J.R. (1970). Cryptococcus neoformans IV. The Not-So-
1405 Encapsulated Yeast. Infect Immun *1*, 526-531.
1406 Feldmesser, M., Kress, Y., and Casadevall, A. (2001). Dynamic changes in the morphology of
1407 *Cryptococcus neoformans* during murine pulmonary infection. Microbiology *147*, 2355-
1408 2365.
1409 Feldmesser, M., Kress, Y., Novikoff, P., and Casadevall, A. (2000). *Cryptococcus neoformans* Is
1410 a facultative intracellular pathogen in murine pulmonary infection. Infect Immun *68*,
1411 4225-4237.
1412 Fernandes, K.E., Brockway, A., Haverkamp, M., Cuomo, C.A., van Ogtrop, F., Perfect, J.R., and
1413 Carter, D.A. (2018). Phenotypic Variability Correlates with Clinical Outcome in
1414 Cryptococcus Isolates Obtained from Botswanan HIV/AIDS Patients. mBio *9*.
1415 Fernandes, K.E., and Carter, D.A. (2020). Cellular plasticity of pathogenic fungi during
1416 infection. PLoS Pathog *16*, e1008571.
1417 Fernandes, K.E., Dwyer, C., Campbell, L.T., and Carter, D.A. (2016). Species in the
1418 Cryptococcus gattii Complex Differ in Capsule and Cell Size following Growth under
1419 Capsule-Inducing Conditions. mSphere *1*.
1420 Garfoot, A.L., Shen, Q., Wüthrich, M., Klein, B.S., and Rappleye, C.A. (2016). The Eng1 β-
1421 Glucanase Enhances Histoplasma Virulence by Reducing β-Glucan Exposure. mBio *7*,
1422 e01388-01315.
1423 Gault, W.J., Enyedi, B., and Niethammer, P. (2014). Osmotic surveillance mediates rapid wound
1424 closure through nucleotide release. J Cell Biol *207*, 767-782.
1425 Gaylord, E.A., Choy, H.L., and Doering, T.L. (2020). Dangerous Liaisons: Interactions of
1426 Cryptococcus neoformans with Host Phagocytes. Pathogens *9*.
1427 Gerstein, A.C., Fu, M.S., Mukaremera, L., Li, Z., Ormerod, K.L., Fraser, J.A., Berman, J., and
1428 Nielsen, K. (2015). Polyploid titan cells produce haploid and aneuploid progeny to
1429 promote stress adaptation. mBio *6*, e01340.
1430 Geunes-Boyer, S., Beers, M.F., Perfect, J.R., Heitman, J., and Wright, J.R. (2012). Surfactant
1431 protein D facilitates *Cryptococcus neoformans* infection. Infect Immun *80*, 2444-2453.
1432 Goldman, D.L., Khine, H., Abadi, J., Lindenberg, D.J., Pirofski, L., Niang, R., and Casadevall,
1433 A. (2001). Serologic evidence for *Cryptococcus neoformans* infection in early childhood.
1434 Pediatrics *107*, E66.
1435 Gow, N.A., Netea, M.G., Munro, C.A., Ferwerda, G., Bates, S., Mora-Montes, H.M., Walker, L.,
1436 Jansen, T., Jacobs, L., Tsoni, V.*, et al.* (2007). Immune recognition of Candida albicans
1437 beta-glucan by dectin-1. J Infect Dis *196*, 1565-1571.
1438 Gow, N.A.R., Latge, J.P., and Munro, C.A. (2017). The Fungal Cell Wall: Structure,
1439 Biosynthesis, and Function. Microbiol Spectr *5*.
1440 Grygorczyk, R., Boudreault, F., Ponomarchuk, O., Tan, J.J., Furuya, K., Goldgewicht, J.,
1441 Kenfack, F.D., and Yu, F. (2021). Lytic Release of Cellular ATP: Physiological
1442 Relevance and Therapeutic Applications. Life (Basel) *11*.
1443 Guimarães, A.J., de Cerqueira, M.D., and Nosanchuk, J.D. (2011). Surface architecture of
1444 histoplasma capsulatum. Front Microbiol *2*, 225.

1445 Haas, R., and Meyer, T.F. (1986). The repertoire of silent pilus genes in Neisseria gonorrhoeae:
1446 evidence for gene conversion. Cell *44*, 107-115.
1447 Harris, G., Davies, J.W., and Parsons, R. (1958). Nucleotide pool of brewers' yeast during
1448 growth and fermentation. Nature *182*, 1565-1567.
1449 Hasan, M.M., Hasan, M.M., Teixeira da Silva, J.A., and Li, X. (2016). Regulation of phosphorus
1450 uptake and utilization: transitioning from current knowledge to practical strategies. Cell
1451 Mol Biol Lett *21*, 7.
1452 Himmelreich, U., Allen, C., Dowd, S., Malik, R., Shehan, B.P., Mountford, C., and Sorrell, T.C.
1453 (2003). Identification of metabolites of importance in the pathogenesis of pulmonary
1454 cryptococcoma using nuclear magnetic resonance spectroscopy. Microbes and Infection
1455 *5*, 285-290.
1456 Hohl, T.M., Van Epps, H.L., Rivera, A., Morgan, L.A., Chen, P.L., Feldmesser, M., and Pamer,
1457 E.G. (2005). Aspergillus fumigatus triggers inflammatory responses by stage-specific
1458 beta-glucan display. PLoS Pathog *1*, e30.
1459 Homer, C.M., Summers, D.K., Goranov, A.I., Clarke, S.C., Wiesner, D.L., Diedrich, J.K.,
1460 Moresco, J.J., Toffaletti, D., Upadhya, R., Caradonna, I.*, et al.* (2016). Intracellular
1461 Action of a Secreted Peptide Required for Fungal Virulence. Cell Host Microbe *19*, 849-
1462 864.
1463 Hommel, B., Mukaremera, L., Cordero, R.J.B., Coelho, C., Desjardins, C.A., Sturny-Leclère, A.,
1464 Janbon, G., Perfect, J.R., Fraser, J.A., Casadevall, A.*, et al.* (2018). Titan cells formation
1465 in Cryptococcus neoformans is finely tuned by environmental conditions and modulated
1466 by positive and negative genetic regulators. PLoS Pathog *14*, e1006982.
1467 Hood, M.I., and Skaar, E.P. (2012). Nutritional immunity: transition metals at the pathogen-host
1468 interface. Nature Reviews Microbiology *10*, 525-537.
1469 Huang, S.H., Long, M., Wu, C.H., Kwon-Chung, K.J., Chang, Y.C., Chi, F., Lee, S., and Jong,
1470 A. (2011). Invasion of Cryptococcus neoformans into human brain microvascular
1471 endothelial cells is mediated through the lipid rafts-endocytic pathway via the dual
1472 specificity tyrosine phosphorylation-regulated kinase 3 (DYRK3). J Biol Chem *286*,
1473 34761-34769.
1474 Ikeh, M.A., Kastora, S.L., Day, A.M., Herrero-de-Dios, C.M., Tarrant, E., Waldron, K.J., Banks,
1475 A.P., Bain, J.M., Lydall, D., Veal, E.A.*, et al.* (2016). Pho4 mediates phosphate
1476 acquisition in *Candida albicans* and is vital for stress resistance and metal homeostasis.
1477 Mol Biol Cell *27*, 2784-2801.
1478 Jacobs, C.W., Adams, A.E., Szaniszlo, P.J., and Pringle, J.R. (1988). Functions of microtubules
1479 in the Saccharomyces cerevisiae cell cycle. J Cell Biol *107*, 1409-1426.
1480 Kanetsuna, F., and Carbonell, L.M. (1971). Cell wall composition of the yeastlike and mycelial
1481 forms of Blastomyces dermatitidis. J Bacteriol *106*, 946-948.
1482 Kim, K. (2012). Malaria var gene expression: keeping up with the neighbors. Cell Host Microbe
1483 *11*, 1-2.
1484 Kohler, J.R., Acosta-Zaldivar, M., and Qi, W. (2020). Phosphate in Virulence of Candida
1485 albicans and Candida glabrata. J Fungi (Basel) *6*, 40.
1486 Kowalski, C.H., Kerkaert, J.D., Liu, K.W., Bond, M.C., Hartmann, R., Nadell, C.D., Stajich,
1487 J.E., and Cramer, R.A. (2019). Fungal biofilm morphology impacts hypoxia fitness and
1488 disease progression. Nat Microbiol *4*, 2430-2441.

1489 Kretschmer, M., Reiner, E., Hu, G., Tam, N., Oliveira, D.L., Caza, M., Yeon, J.H., Kim, J.,
1490 Kastrup, C.J., Jung, W.H., *et al.* (2014). Defects in phosphate acquisition and storage
1491 influence virulence of Cryptococcus neoformans. Infect Immun *82*, 2697-2712.
1492 Kubes, P., and Jenne, C. (2018). Immune Responses in the Liver. Annu Rev Immunol *36*, 247-
1493 277.
1494 Lazera, M.S., Pires, F.D., Camillo-Coura, L., Nishikawa, M.M., Bezerra, C.C., Trilles, L., and
1495 Wanke, B. (1996). Natural habitat of *Cryptococcus neoformans var. neoformans* in
1496 decaying wood forming hollows in living trees. J Med Vet Mycol *34*, 127-131.
1497 Lee, H., Chang, Y.C., Nardone, G., and Kwon-Chung, K.J. (2007). TUP1 disruption in
1498 *Cryptococcus neoformans* uncovers a peptide-mediated density-dependent growth
1499 phenomenon that mimics quorum sensing. Mol Microbiol *64*, 591-601.
1500 Lee, S.C., Dickson, D.W., and Casadevall, A. (1996). Pathology of cryptococcal
1501 meningoencephalitis: analysis of 27 patients with pathogenetic implications. Hum Pathol
1502 *27*, 839-847.
1503 Lev, S., and Djordjevic, J.T. (2018). Why is a functional PHO pathway required by fungal
1504 pathogens to disseminate within a phosphate-rich host: A paradox explained by alkaline
1505 pH-simulated nutrient deprivation and expanded PHO pathway function. PLoS Pathog
1506 *14*, e1007021.
1507 Lev, S., Kaufman-Francis, K., Desmarini, D., Juillard, P.G., Li, C., Stifter, S.A., Feng, C.G.,
1508 Sorrell, T.C., Grau, G.E., Bahn, Y.S., *et al.* (2017). Pho4 Is Essential for Dissemination
1509 of Cryptococcus neoformans to the Host Brain by Promoting Phosphate Uptake and
1510 Growth at Alkaline pH. mSphere *2*.
1511 Li, P.Z., Li, J.Z., Li, M., Gong, J.P., and He, K. (2014). An efficient method to isolate and
1512 culture mouse Kupffer cells. Immunol Lett *158*, 52-56.
1513 Li, Z., and Nielsen, K. (2017). Morphology Changes in Human Fungal Pathogens upon
1514 Interaction with the Host. J Fungi (Basel) *3*, 66.
1515 Liao, Y., Smyth, G.K., and Shi, W. (2014). featureCounts: an efficient general purpose program
1516 for assigning sequence reads to genomic features. Bioinformatics *30*, 923-930.
1517 Lim, J., Coates, C.J., Seoane, P.I., Garelnabi, M., Taylor-Smith, L.M., Monteith, P., Macleod,
1518 C.L., Escaron, C.J., Brown, G.D., Hall, R.A., *et al.* (2018). Characterizing the
1519 Mechanisms of Nonopsonic Uptake of Cryptococci by Macrophages. J Immunol *200*,
1520 3539-3546.
1521 Lin, Y.Y., Shiau, S., and Fang, C.T. (2015). Risk factors for invasive *Cryptococcus neoformans*
1522 diseases: a case-control study. PLoS One *10*, e0119090.
1523 Liu, N.N., Uppuluri, P., Broggi, A., Besold, A., Ryman, K., Kambara, H., Solis, N., Lorenz, V.,
1524 Qi, W., Acosta-Zaldivar, M., *et al.* (2018). Intersection of phosphate transport, oxidative
1525 stress and TOR signalling in *Candida albicans* virulence. PLoS Pathog *14*, e1007076.
1526 Liu, T.B., Kim, J.C., Wang, Y., Toffaletti, D.L., Eugenin, E., Perfect, J.R., Kim, K.J., and Xue,
1527 C. (2013). Brain inositol is a novel stimulator for promoting Cryptococcus penetration of
1528 the blood-brain barrier. PLoS Pathog *9*, e1003247.
1529 Liu, T.B., Subbian, S., Pan, W., Eugenin, E., Xie, J., and Xue, C. (2014). Cryptococcus inositol
1530 utilization modulates the host protective immune response during brain infection. Cell
1531 Communication and Signaling *12*, 51.
1532 López-Fuentes, E., Gutiérrez-Escobedo, G., Timmermans, B., Van Dijck, P., De Las Peñas, A.,
1533 and Castaño, I. (2018). Candida glabrata's Genome Plasticity Confers a Unique Pattern of
1534 Expressed Cell Wall Proteins. J Fungi (Basel) *4*.

1535 Love, M.I., Huber, W., and Anders, S. (2014). Moderated estimation of fold change and
1536 dispersion for RNA-seq data with DESeq2. Genome Biol *15*, 550.
1537 Luberto, C., Martinez-Marino, B., Taraskiewicz, D., Bolanos, B., Chitano, P., Toffaletti, D.L.,
1538 Cox, G.M., Perfect, J.R., Hannun, Y.A., Balish, E.*, et al.* (2003). Identification of App1
1539 as a regulator of phagocytosis and virulence of *Cryptococcus neoformans*. J Clin Invest
1540 *112*, 1080-1094.
1541 Macpherson, A.J., Heikenwalder, M., and Ganal-Vonarburg, S.C. (2016). The Liver at the Nexus
1542 of Host-Microbial Interactions. Cell Host Microbe *20*, 561-571.
1543 Martin, M. (2011). Cutadapt removes adapter sequences from high-throughput sequencing reads.
1544 EMBnet *17*, 10-12.
1545 Maruvada, R., Zhu, L., Pearce, D., Zheng, Y., Perfect, J., Kwon-Chung, K.J., and Kim, K.S.
1546 (2012). Cryptococcus neoformans phospholipase B1 activates host cell Rac1 for traversal
1547 across the blood-brain barrier. Cell Microbiol *14*, 1544-1553.
1548 Maziarz, E.K., and Perfect, J.R. (2016). Cryptococcosis. Infect Dis Clin North Am *30*, 179-206.
1549 Mukaremera, L., Lee, K.K., Mora-Montes, H.M., and Gow, N.A.R. (2017). Candida albicans
1550 Yeast, Pseudohyphal, and Hyphal Morphogenesis Differentially Affects Immune
1551 Recognition. Front Immunol *8*, 629.
1552 Mukaremera, L., McDonald, T.R., Nielsen, J.N., Molenaar, C.J., Akampurira, A., Schutz, C.,
1553 Taseera, K., Muzoora, C., Meintjes, G., Meya, D.B.*, et al.* (2019). The Mouse Inhalation
1554 Model of Cryptococcus neoformans Infection Recapitulates Strain Virulence in Humans
1555 and Shows that Closely Related Strains Can Possess Differential Virulence. Infect Immun
1556 *87*, e00046-00019.
1557 Ngamskulrungroj, P., Chang, Y., Sionov, E., and Kwon-Chung, K.J. (2012). The primary target
1558 organ of *Cryptococcus gattii* is different from that of *Cryptococcus neoformans* in a
1559 murine model. mBio *3*, e00103-00112.
1560 O'Meara, T.R., and Alspaugh, J.A. (2012). The *Cryptococcus neoformans* capsule: a sword and a
1561 shield. Clin Microbiol Rev *25*, 387-408.
1562 Okagaki, L.H., and Nielsen, K. (2012). Titan cells confer protection from phagocytosis in
1563 Cryptococcus neoformans infections. Eukaryot Cell *11*, 820-826.
1564 Okagaki, L.H., Strain, A.K., Nielsen, J.N., Charlier, C., Baltes, N.J., Chrétien, F., Heitman, J.,
1565 Dromer, F., and Nielsen, K. (2010). Cryptococcal cell morphology affects host cell
1566 interactions and pathogenicity. PLoS Pathog *6*, e1000953-e1000953.
1567 Okagaki, L.H., Wang, Y., Ballou, E.R., O'Meara, T.R., Bahn, Y.-S., Alspaugh, J.A., Xue, C., and
1568 Nielsen, K. (2011). Cryptococcal titan cell formation is regulated by G-protein signaling
1569 in response to multiple stimuli. Eukaryot Cell *10*, 1306-1316.
1570 Olszewski, M.A., Noverr, M.C., Chen, G.H., Toews, G.B., Cox, G.M., Perfect, J.R., and
1571 Huffnagle, G.B. (2004). Urease expression by Cryptococcus neoformans promotes
1572 microvascular sequestration, thereby enhancing central nervous system invasion. Am J
1573 Pathol *164*, 1761-1771.
1574 Otero, X.L., De La Peña-Lastra, S., Pérez-Alberti, A., Ferreira, T.O., and Huerta-Diaz, M.A.
1575 (2018). Seabird colonies as important global drivers in the nitrogen and phosphorus
1576 cycles. Nat Commun *9*, 246.
1577 Pande, K., Chen, C., and Noble, S.M. (2013). Passage through the mammalian gut triggers a
1578 phenotypic switch that promotes Candida albicans commensalism. Nat Genet *45*, 1088-
1579 1091.

1580 Panepinto, J.C., Komperda, K.W., Hacham, M., Shin, S., Liu, X., and Williamson, P.R. (2007).
1581 Binding of serum mannan binding lectin to a cell integrity-defective *Cryptococcus*
1582 *neoformans* ccr4Delta mutant. Infect Immun *75*, 4769-4779.
1583 Pearson, A.M., Rich, A., and Krieger, M. (1993). Polynucleotide binding to macrophage
1584 scavenger receptors depends on the formation of base-quartet-stabilized four-stranded
1585 helices. J Biol Chem *268*, 3546-3554.
1586 Rajasingham, R., Smith, R.M., Park, B.J., Jarvis, J.N., Govender, N.P., Chiller, T.M., Denning,
1587 D.W., Loyse, A., and Boulware, D.R. (2017). Global burden of disease of HIV-associated
1588 cryptococcal meningitis: an updated analysis. Lancet Infect Dis *17*, 873-881.
1589 Ren, H., Teng, Y., Tan, B., Zhang, X., Jiang, W., Liu, M., Jiang, W., Du, B., and Qian, M.
1590 (2014). Toll-like receptor-triggered calcium mobilization protects mice against bacterial
1591 infection through extracellular ATP release. Infect Immun *82*, 5076-5085.
1592 Rivera, J., Feldmesser, M., Cammer, M., and Casadevall, A. (1998). Organ-Dependent Variation
1593 of Capsule Thickness in Cryptococcus neoformans during Experimental Murine
1594 Infection. Infect Immun *66*, 5027-5030.
1595 Roberts, D.J., Craig, A.G., Berendt, A.R., Pinches, R., Nash, G., Marsh, K., and Newbold, C.I.
1596 (1992). Rapid switching to multiple antigenic and adhesive phenotypes in malaria. Nature
1597 *357*, 689-692.
1598 Sabiiti, W., May, R.C., and Pursall, E.R. (2012). Experimental models of cryptococcosis. Int J
1599 Microbiol *2012*, 626745.
1600 Sahly, H., Ofek, I., Podschun, R., Brade, H., He, Y., Ullmann, U., and Crouch, E. (2002).
1601 Surfactant protein D binds selectively to Klebsiella pneumoniae lipopolysaccharides
1602 containing mannose-rich O-antigens. J Immunol *169*, 3267-3274.
1603 San Juan, B.P., Garcia-Leon, M.J., Rangel, L., Goetz, J.G., and Chaffer, C.L. (2019). The
1604 Complexities of Metastasis. Cancers (Basel) *11*, 1575.
1605 Santiago-Tirado, F.H., Onken, M.D., Cooper, J.A., Klein, R.S., and Doering, T.L. (2017). Trojan
1606 Horse Transit Contributes to Blood-Brain Barrier Crossing of a Eukaryotic Pathogen.
1607 mBio *8*.
1608 Selmecki, A.M., Maruvka, Y.E., Richmond, P.A., Guillet, M., Shoresh, N., Sorenson, A.L., De,
1609 S., Kishony, R., Michor, F., Dowell, R.*, et al.* (2015). Polyploidy can drive rapid
1610 adaptation in yeast. Nature *519*, 349-352.
1611 Smith, J.D., Chitnis, C.E., Craig, A.G., Roberts, D.J., Hudson-Taylor, D.E., Peterson, D.S.,
1612 Pinches, R., Newbold, C.I., and Miller, L.H. (1995). Switches in expression of
1613 Plasmodium falciparum var genes correlate with changes in antigenic and cytoadherent
1614 phenotypes of infected erythrocytes. Cell *82*, 101-110.
1615 Stajich, J.E., Harris, T., Brunk, B.P., Brestelli, J., Fischer, S., Harb, O.S., Kissinger, J.C., Li, W.,
1616 Nayak, V., Pinney, D.F.*, et al.* (2012). FungiDB: an integrated functional genomics
1617 database for fungi. Nucleic Acids Res *40*, D675-681.
1618 Stano, P., Williams, V., Villani, M., Cymbalyuk, E.S., Qureshi, A., Huang, Y., Morace, G.,
1619 Luberto, C., Tomlinson, S., and Del Poeta, M. (2009). App1: an antiphagocytic protein
1620 that binds to complement receptors 3 and 2. J Immunol *182*, 84-91.
1621 Sun, D., Sun, P., Li, H., Zhang, M., Liu, G., Strickland, A.B., Chen, Y., Fu, Y., Xu, J., Yosri, M.*,*
1622 *et al.* (2019). Fungal dissemination is limited by liver macrophage filtration of the blood.
1623 Nat Commun *10*, 4566.

1624 Sun, D., Zhang, M., Liu, G., Wu, H., Li, C., Zhou, H., Zhang, X., and Shi, M. (2016).
1625 Intravascular clearance of disseminating *Cryptococcus neoformans* in the brain can be
1626 improved by enhancing neutrophil recruitment in mice. Eur J Immunol *46*, 1704-1714.
1627 Swanson, J., Bergström, S., Robbins, K., Barrera, O., Corwin, D., and Koomey, J.M. (1986).
1628 Gene conversion involving the pilin structural gene correlates with pilus+ in equilibrium
1629 with pilus- changes in Neisseria gonorrhoeae. Cell *47*, 267-276.
1630 Tao, L., Du, H., Guan, G., Dai, Y., Nobile, C.J., Liang, W., Cao, C., Zhang, Q., Zhong, J., and
1631 Huang, G. (2014). Discovery of a "white-gray-opaque" tristable phenotypic switching
1632 system in candida albicans: roles of non-genetic diversity in host adaptation. PLoS Biol
1633 *12*, e1001830.
1634 Todd, R.T., Braverman, A.L., and Selmecki, A. (2018). Flow Cytometry Analysis of Fungal
1635 Ploidy. Curr Protoc Microbiol *50*, e58-e58.
1636 Trevijano-Contador, N., de Oliveira, H.C., García-Rodas, R., Rossi, S.A., Llorente, I., Zaballos,
1637 Á., Janbon, G., Ariño, J., and Zaragoza, Ó. (2018). Cryptococcus neoformans can form
1638 titan-like cells in vitro in response to multiple signals. PLoS Pathog *14*, e1007007.
1639 van der Woude, M.W., and Bäumler, A.J. (2004). Phase and antigenic variation in bacteria. Clin
1640 Microbiol Rev *17*, 581-611, table of contents.
1641 Viriyakosol, S., Singhania, A., Fierer, J., Goldberg, J., Kirkland, T.N., and Woelk, C.H. (2013).
1642 Gene expression in human fungal pathogen Coccidioides immitis changes as
1643 arthroconidia differentiate into spherules and mature. BMC Microbiol *13*, 121.
1644 Vu, K., Eigenheer, R.A., Phinney, B.S., and Gelli, A. (2013). Cryptococcus neoformans
1645 promotes its transmigration into the central nervous system by inducing molecular and
1646 cellular changes in brain endothelial cells. Infect Immun *81*, 3139-3147.
1647 Walsh, N.M., Botts, M.R., McDermott, A.J., Ortiz, S.C., Wüthrich, M., Klein, B., and Hull, C.M.
1648 (2019). Infectious particle identity determines dissemination and disease outcome for the
1649 inhaled human fungal pathogen Cryptococcus. PLoS Pathog *15*, e1007777.
1650 Wang, L., and Lin, X. (2015). The morphotype heterogeneity in *Cryptococcus neoformans*. Curr
1651 Opin Microbiol *26*, 60-64.
1652 Wang, L., Zhai, B., and Lin, X. (2012). The link between morphotype transition and virulence in
1653 *Cryptococcus neoformans*. PLoS Pathog *8*, e1002765.
1654 Ward, C.P., Clottey, G.T., Dorris, M., Ji, D.D., and Arnot, D.E. (1999). Analysis of Plasmodium
1655 falciparum PfEMP-1/var genes suggests that recombination rearranges constrained
1656 sequences. Mol Biochem Parasitol *102*, 167-177.
1657 Weigel, W.A., and Dersch, P. (2018). Phenotypic heterogeneity: a bacterial virulence strategy.
1658 Microbes Infect *20*, 570-577.
1659 Whiston, E., Zhang Wise, H., Sharpton, T.J., Jui, G., Cole, G.T., and Taylor, J.W. (2012).
1660 Comparative transcriptomics of the saprobic and parasitic growth phases in Coccidioides
1661 spp. PLoS One *7*, e41034.
1662 Wozniak, K.L., and Levitz, S.M. (2009). Isolation and purification of antigenic components of
1663 *Cryptococcus*. Methods Mol Biol *470*, 71-83.
1664 Wright, L., Bubb, W., Davidson, J., Santangelo, R., Krockenberger, M., Himmelreich, U., and
1665 Sorrell, T. (2002). Metabolites released by *Cryptococcus neoformans var. neoformans*
1666 and *var. gattii* differentially affect human neutrophil function. Microbes Infect *4*, 1427-
1667 1438.

1668 Xie, S., Sao, R., Braun, A., and Bottone, E.J. (2012). Difference in Cryptococcus neoformans
1669 cellular and capsule size in sequential pulmonary and meningeal infection: a postmortem
1670 study. Diagnostic Microbiology and Infectious Disease *73*, 49-52.
1671 Yoneda, A., and Doering, T.L. (2006). A eukaryotic capsular polysaccharide is synthesized
1672 intracellularly and secreted via exocytosis. Mol Biol Cell *17*, 5131-5140.
1673 Zaragoza, O. (2011). Multiple Disguises for the Same Party: The Concepts of Morphogenesis
1674 and Phenotypic Variations in Cryptococcus neoformans. Front Microbiol *2*, 181.
1675 Zaragoza, O., García-Rodas, R., Nosanchuk, J.D., Cuenca-Estrella, M., Rodríguez-Tudela, J.L.,
1676 and Casadevall, A. (2010). Fungal cell gigantism during mammalian infection. PLoS
1677 Pathog *6*, e1000945-e1000945.
1678 Zhang, M., Sun, D., Liu, G., Wu, H., Zhou, H., and Shi, M. (2016). Real-time *in vivo* imaging
1679 reveals the ability of neutrophils to remove *Cryptococcus neoformans* directly from the
1680 brain vasculature. J Leukoc Biol *99*, 467-473.
1681 Zhou, X., and Ballou, E.R. (2018). The Cryptococcus neoformans Titan Cell: From In Vivo
1682 Phenomenon to In Vitro Model. Current Clinical Microbiology Reports *5*, 252-260.
1683 Zhou, X., Zafar, H., Sephton-Clark, P., Mohamed, S.H., Chapuis, A., Makarova, M.,
1684 MacCallum, D.M., Drummond, R.A., Dambuza, I.M., and Ballou, E.R. (2020). Host
1685 environmental conditions induce small fungal cell size and alter population heterogeneity
1686 in *Cryptococcus neoformans*. bioRxiv, 2020.2001.2003.894709.
1687